Probing Underlying Processes in Organic Photovoltaics with Atomic Force Microscopies

Guozheng Shao

A dissertation

submitted in partial fulfillment of the

requirements for the degree of

Doctor of Philosophy

University of Washington

2014

Reading Committee:

David S. Ginger, Chair

Charles T. Campbell

Samson A. Jenekhe

Program Authorized to Offer Degree:

Department of Chemistry

University of Washignton

Abstract

Probing Underlying Processes in Organic Photovoltaics with Atomic Force Microscopies

Guozheng Shao

Department of Chemistry

Photovoltaic is one potential solution to the ever growing demand of energy of our society. Making plastics absorb sunlight in order to generate electricity is a surprisingly easy process. However, fabricating *efficient* plastic solar cells is another story.

A typical organic solar cell is made by blending the electron donor (polymer) and acceptor materials (fullerene derivatives) together and spin coat the solution on top of a transparent electrode to make a thin film (a process like making crêpe). No wonder that the micro-morphology determines all the key parameters of a completed device such as open circuit voltage, short circuit current, fill factor and lifetime.

Atomic Force Microscopy is one unique tool to study the optoelectronic processes in organic photovoltaics (OPV), for it allows one to study the local morphology and electronic properties, *e.g.* photocurrent, carrier mobilities, charging rate, at the same time.

I have shown in this dissertation the properties of OPV that could hardly be learned otherwise. In Chapter 1, I summarize recent thinking the OPV field and speculate on possible research

projects. In Chapter 2, with the blend of PFB:F8BT, I demonstrate that the breakdown of the most sensitive part in an OPV, percolation pathway, would lead to the degradation of the whole area. In Chapter 3, I am showing a technique that I have been developing, frequency modulated Scanning Kelvin Probe Microscopy (FM-SKPM), to study the charge carrier lifetime at the buried interface in an OPV device. The application of this technique will be demonstrated on a patterned indium tin oxide surface with alternating phosphonic acids with different work functions.

TABLE OF CONTENTS

LIST OF FIGURES

LIST OF TABLES

ACKNOWLEDGEMENTS

This dissertation could not have been done without the support and inspiration of many people from my family to my friends, teachers and advisors at different stages. First and foremost, I would like to thank my advisor, Professor David S. Ginger, for his support and passion for science, I could have done none of these work all on my own.

I also want to thank Dr. Cody W. Schlenker for many inspirational discussions. Being extremely helpful and conscientious, Cody totally expanded my view on scientific study and literature. Then I want to express my appreciation to Dr. Hao Sun who helped me started in a research project.

I owe very much of my achievements to my parents and sisters. They are always there to provide me with unconditional support.

Many people contributed to this work. Dr. Cody W. Schlenker and Dr. Michael Salvador provided critical views on Chapter 1. Eric M. Smith helped me carry out some of the GATR-FTIR measurements in Chapter 2. For Chapter 3, Dr. Micah S. Glaz prepared many samples and spent a lot of long hours in front of AFM to take the data. Dr. Fei Ma and Huanxin Ju have been very helpful in taking TPV data for me. Every member of Ginger Group has always been very helpful with technical problems.

I would personally thank my friend and teacher of badminton at University of Washington, Fangmao Ye, for sharing his experiences and wisdoms with me.

Part of the work done here is supported by National Science Foundation. My travels to meetings have been supported by Department of Chemistry and Graduate School at University of Washington.

DEDICATION

To my wife, Xiaojuan Liu.

Chapter 1

Limitations and Variables in Organic Photovoltaics

1.1 Introduction

Among the many challenges our society faces today, a reliable source of renewable energy is one of the most pressing topics. Photovoltaics have been a vital part in the endeavor of adopting clean energy solutions. Various types of thin-film solar cells such as inorganic semiconductor-based solar cells, dye-sensitized solar cells, and polymer based organic photovoltaics (OPVs) have been studied for the past decade yielding tremendous advances in light-to-current conversion rates. Currently, all these sub-types of solar cells have passed 10% in their power conversion efficiency. Compared to their silicon-based counterparts, the unique advantage of OPVs is their potential for low cost and scalability in mass production. Besides the challenge of extending the efficiency horizon further through the discovery of new organic semiconductor materials and innovative device fabrication protocols, understanding and controlling the relationship between microscopic structural composition and the underlying physics of device performance is an essential prerequisite for elevating this technology to the next level. We provide a new perspective on fundamental processes of OPV performance based on excitingly new experimental results.

As energy harvesting schemes based on tandem cells[1-3] and hybrid cells[4, 5] have passed power conversion efficiencies of 10% by absorbing a larger portion of the solar spectrum, we are more

encouraged to understand photophysics and fabricate OPV with even higher performance. Various studies have shown that experimental conditions such as the choice of solvent/additives,[6, 7] annealing (if applied) and post-processing conditions[8, 9] all lead to variations in V_{oc}, J_{sc}, FF, and, consequently, in the overall power conversion efficiency. Hence, a good understanding of the tunable material and device variables is important for defining successful research strategies.

Inorganic solar cells are generally accepted as the "better" performing devices. One means of understanding the discrepancy in device performance of different photovoltaic technologies is by comparing the highest measured V_{oc} that is attainable for a given band gap. Figure 1.1 shows this comparison for several inorganic and organic photovoltaic devices.[6, 10-16] For inorganic solar cells, excitons dissociate directly after photon absorption with no extra energy loss other than thermalization of the excited exciton. With the exception of CZTS, V_{oc} for inorganic cells follows the bandgap very closely. However, organic solar cells deviate from this trend due to the typically much lower dielectric constants of the OPV blend. Light absorption in organic solar cells produces a tightly bound Frenkel exciton rather than free moving electron-hole pairs with a binding energy ~0.5 eV.[17] This energy can only be surpassed with extra thrust. Empirically, differences between V_{oc} and the effective band gap, i.e., $(E_{LUMO,\ acceptor} - E_{HOMO,\ donor})/q$, have been determined to be ~ 0.6 V.[18] This voltage loss of 0.6 V can be decomposed in different ways, such as into a sum of the loss before and after the event of charge transfer state formation. The latter was considered as a sheer loss of energy that could be harnessed in the ideal case. It has been suggested that shrinking this total loss to ~ 0.2 V could raise the modified Shockley-Queisser limit for OPVs to 22%.[17]

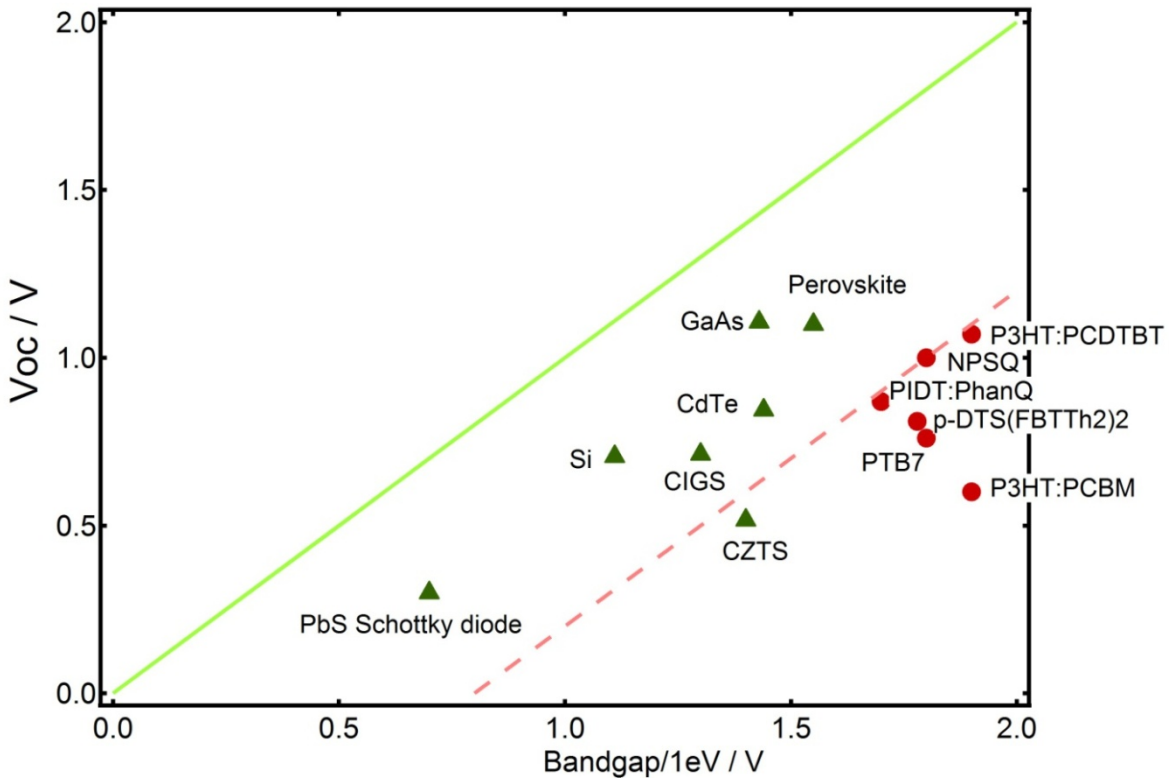

Figure 1.1. Blue dashed and red dotted lines are guides to the eye. Green triangles are for inorganic solar cells, red dots are for organic cells, specifically, P3HT:PCDTBT, NPSQ, p-DTS(FBTTh2)$_2$, PIDT:PhanQ, P3HT:PCBM, PTB7. Inorganic solar cells deviates from the ideal V_{oc} due to non-radiative recombination. Organic solar cells drop even lower due to the extra columbic attraction between hole and electron.

Besides energy loss during charge separation, the separation of charges is also more difficult due to the smaller delocalization length. State-of-the-art OPV devices are prepared to form a bulk heterojunction (BHJ) structure, where the electron donor and acceptor materials are finely blended in order to maximize the interface between them and, therefore, facilitate exciton separation and charge transport. The source and sink for charges in an OPV device are highly

dependent on the microscopic structure of the film and the energy of materials involved. Yet morphology and energy levels are largely interdependent. For instance, morphology as a manifestation of microscopic or even molecular aggregation may determine the size of the bandgap and furthermore the alignment of frontier orbitals and energy levels. Electronic interaction on the other hand may affect the molecular packing and, therefore, the blend morphology, as shown in recent examples.[19, 20]

Despite of the fact that PCE remains at ~10% in state-of-the-art devices, many different schemes have been proposed towards the goal of above 20% PCE,[21, 22] yet creating many controversies regarding energy level considerations and the structural morphology of the film.[23, 24] This review serves as a summary and an analysis of recent developments in understanding the role of morphology in charge generation and potential ways for achieving better control of film morphology. Similar to recent statements by Toney and Durrant,[25, 26] who point out that the OPV operation involves a wide range of microscopic scales, and that any single characterization technique on a given sample might not yield a paradigm for all the candidate materials, we believe that the successful description of OPV physics would require different levels of theory as well. We begin this discussion starting from the important concept of charge transfer (CT) state formation.

1.2 Energetics & Charge Transfer State

Donor and acceptor in an OPV device form a type II heterojunction. Charge separation is a driven by loss of free energy. For most cases, the change of enthalpy is the determining factor as we typically compare the LUMO levels to decide whether charge transfer could happen or not.

Controlling for energy level alignments have been an important aspect in material designing for OPV application.

The energy states involved in the photogeneration in a typical OPV device are illustrated in Figure 1.2.[27] A is the exciton state formed directly upon absorption of a photon. B is the charge transfer (CT) state where positive and negative charge resides on the donor and acceptor respectively. C is the exciton state formed by the relaxation of CT state, it could be both singlet and triplet spin in nature. As shown in Figure 1.2, an exciton forms upon electronic excitation of the absorbing chromophore (polymer). The exciton then needs to migrate to the donor/acceptor interface to be able to separate into free charges, utilizing the energy difference of the two materials. Either limited by exciton diffusion or tunneling, the distance it could tranverse is small, on the order of 10 nm / 1 nm,[28-30] respectively. Immediately after exciton splitting at the interface, the still Coulombically bounded electron/hole pair is called a charge transfer (CT) state.

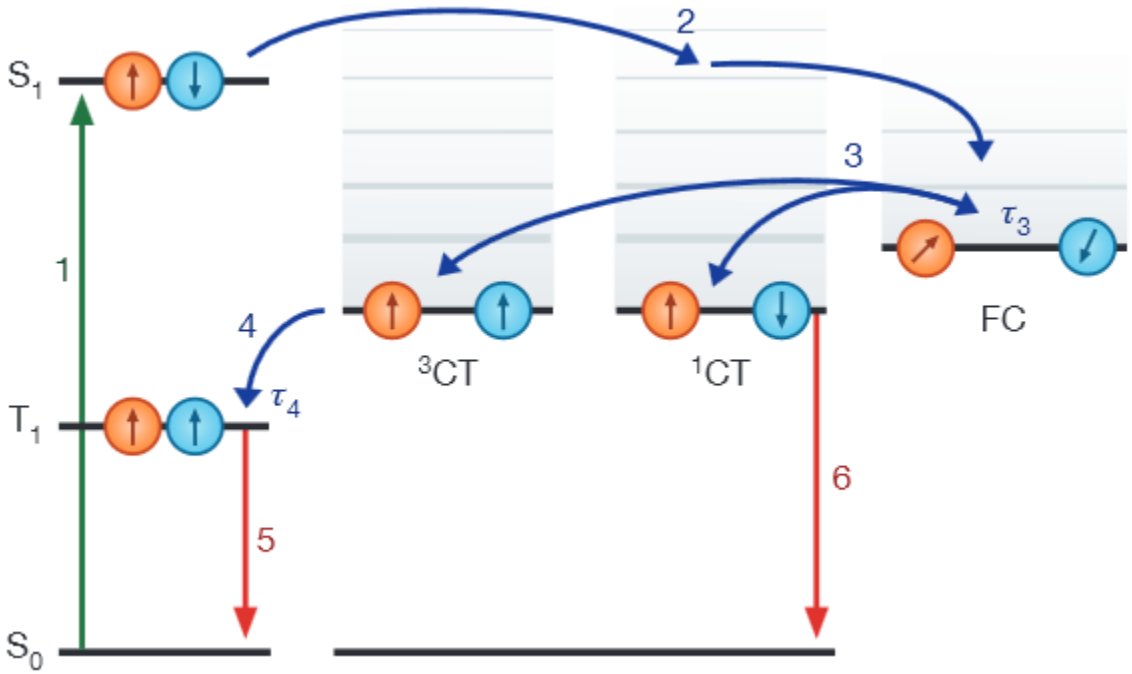

Figure 1.2 should describe all the source, converter and reservoir. Process 1 is the absorption of a photon. 2 is the generation of charge transfer state. 3 is the equilibrium between charge separation and reforming the charge transfer states. 4 means the charge transfer states formation on the polymer itself. 5 is the nonradiative recombination, while 6 is the radiative recombination. Taken from ref[27].

The energy states involved in the photophysics are arranged in such a way that we can view the OPV as of three components from the perspective of exciton conservation: the source, which is the directly photogenerated exciton, with the highest energy in all species that would be discussed; the convertor, which is the CT states that convert closely bounded exciton states into free moving charges, lower in energy than photogenerated exciton; and the reservoir, the relaxed exciton states formed from the relaxation of the large number of incomplete separated free charges, lowest in energy.[27, 31] The relaxed exciton states is comprised of two components, the singlet exciton and the triplet exciton, the former has a rate of decaying back to ground state while the decay of the latter is forbidden due to its spin-state. Given enough thermal energy and delocalization, re-excitation of the exciton states would also generate the CT states.[32]

The CT state precedes the charge separation state, in which the exciton is fully separated into free charges. Lifetime and separation efficiency of CT states determine the efficiency of OPV devices. CT state energy also determines Voc obtainable in an OPV device. The optimal energy offset of donor and acceptor for CT separation follows the predictions of Marcus theory and is thus a function of wavefunction overlap between the wavefunctions of exciton and CT states.[33, 34] In the LUMO energy range of interest, the energy offset is located in the upright Marcus region,

where larger energy offsets lead to more efficient energy transfer, forming more CT states. More efficient CT separation would lead to a higher J_{sc}. On the other hand, smaller energy loss during CT separation means a higher achievable V_{oc}. However, improvements on Jsc and Voc have largely remained mutually exclusive,[35] as shown in Figure 1.3, the blue and red region represent different class of polymers, with the blue region being the polymers used in early study of OPV,[36-38] the red ones are innovated polymer with alternating donor-acceptor strucuture,[10, 13, 16, 39, 40] proposed by Thompson *et al*.[41] The red ones show higher obtainable Jsc at given Voc compared with their precedents, showing the superior charge separation capabilities.

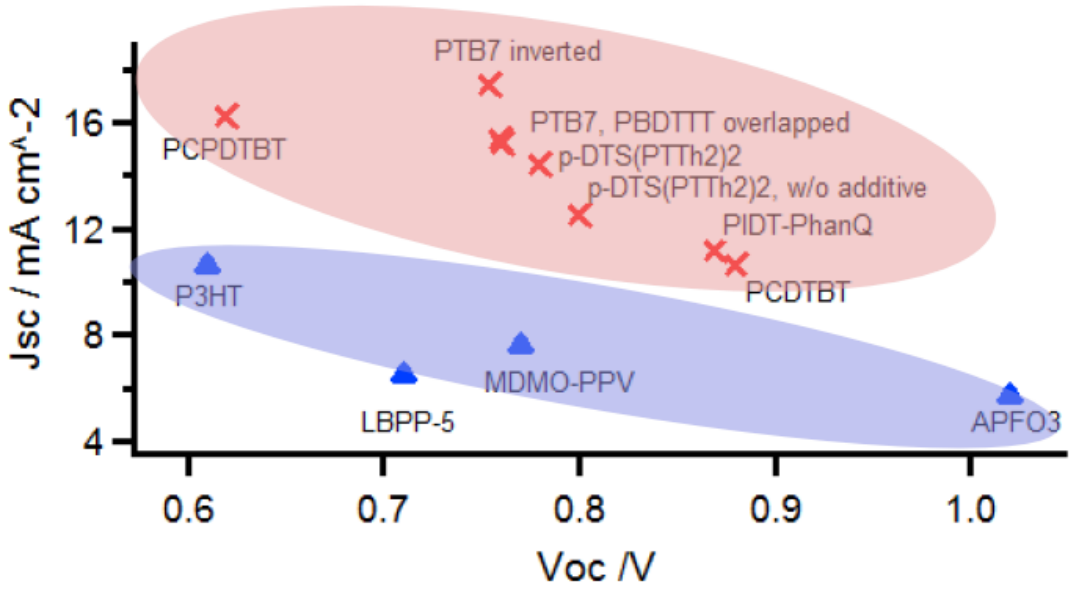

Figure 1.3 Electronic interactions between donor and acceptor. The blue block includes polymers introduced ~ a decade ago, while the red block covers the most recently introduce polymers.

In practice, for CT states to form, singlet exciton needs to at least 0.1 eV higher in energy than CT states.[24] It was tested in 18 combinations of polymer:fullerene blend. The occurrence of CT states formation was evaluated by an overall analysis of the disappearance of singlet photoluminescence, appearance of CT state emission, relative high efficiency of the device and the presence of polaron absorption.

Charge transfer process is limited by the LUMO and HOMO alignments between donor and acceptor. Small LUMO offset will impede electron transfer.[23] When PF10TBT was blended with different fullerene derivatives, photocurrent was found to decrease with increased fullerene LUMO level. Recombination through triplet states on the polymer from fullerene singlets states was accounted for the loss in photocurrent. In the meantime, polaron states on polymer, representing positively charge states, was missing from the photoinduced absorption spectrum in the blend with ICBA, with highest LUMO among all fullerenes used, indicating the lack to electron transfer.

On the other hand, hole transfer could be turned off if HOMO offset between donor and acceptor vanished.[42] In this case, PBTHDDT was tested with different fullerene derivatives. Photoexcitation of the polymer led to positive polaron on the polymer and negative polaron on the fullerenes. However, while excitation of fullerene in the blend with $PC_{61}BM$ and $PC_{71}BM$ both produced long-lived polarons, no discernible PIA signal was observed in the blend of polymer:ICBA. This was attributed to the higher lying HOMO level of ICBA over polymer HOMO level, suggesting HOMO level alignment is also an important parameter for material design.

Lower lying state is not necessarily the gateway for charge recombination. When PIDT-PhanQ was blended with a series of C_{60} and C_{70} based fullerene derivatives.[43] Higher V_{oc} was achieved with higher fullerene LUMO levels, with reduced J_{sc} at the same time. $PC_{71}BM$ blend showed a high photocurrent even the polymer triplet state was more than 300 meV below CT states. PIA spectrum of all the fullerene blends except ICBA showed polaron feature, only the ICBA blend had the extra polymer triplet feature. This polymer triplet feature was a result of Dexter transfer from the ICBA triplet states, indicating the ICBA triplet state was dominating triplet recombination although polymer triplet state was lower in energy.

Meanwhile, energetically favored recombination through polymer triplet states could be avoided with better backbone packing.[44] PCPDTBT was blended with PCBM, with and without diiodooctane (DIO) additive. Despite CT state energy was estimated to be ~0.20 eV above polyme triplet ground state and qualifies well for energy transfer ($E_{CT} - E_T > 0.10$ eV), in the case where DIO additive was used, recombination through polymer triplet states was found to be much lower. This was accounted by the larger aggregates of polymer in TEM.

Traditionally, CT state formation/separation is explained within the frame work of the Onsager-Braun model.[45] However, experimentally observed ultrafast CT separation was several orders of magnitude faster than predicted. This discrepancy has been explained by the local electric field, which could be a result of the donor:acceptor LUMO offset,[24] or due to an interfacial dipole,[46-48] or an energy gradient formed by the crystallinity gradient within donor and acceptor moiety,[49] or even delocalization of CT states over more crystalline regions.[50] However, the simple idea of energetics of the donor:acceptor HOMO/LUMO offset successfully explained origin of V_{oc} in OPV devices. The empirical relation of Voc = gap -0.6 eV holds true for a large library of donor/acceptor materials. Relative energy level alignment of singlet and triplet states

also provides a guideline for describing charge recombination pathways. This reminds us to take into account of all the possible processes such as energy transfer, charge transfer and recombination in designing a novel OPV device. Yet the process inside an OPV device is complicated by the microscopic structure of the film.

Several important questions need to be answered for obtaining a better understanding regarding the role of morphology in organic solar cells. For instance, what is the most desirable morphology, crystalline or amorphous? Is the morphology determined by electronic interactions and can we model morphology formation that takes into account the inherent electronic interactions between donor and acceptor materials? Can we fine-tune the morphology to reach optimal charge separation and generation? We attempt to summarize recent developments towards understanding these questions in the following sections.

1.3 Molecular/Energy Disorder and Energy Gradient

Morphology has been known to play a crucial role in the BHJ structure. The current perception is that the best device performance requires an almost perfect spatial distribution of donor and acceptor phases of different sizes. In some cases, the good device performances were attributed to the microscopic phase segregation, while in other cases experimental results suggested that a larger degree of crystallinity was responsible for enhanced efficiency. A better understanding of the microscopic morphology together/along with device performance could help filter out the key parameters.

A wide range of experimental evidence points to the importance of a ternary phase model for efficient charge separation in OPV devices.[49, 51] This model proposes that a polymer-rich phase

co-exists with a fullerene-rich phase and a mixture consisting of amorphous polymer chains and amorphous fullerenes. Importantly, the mixed phase, i.e. the miscibility of polymer and fullerene, seems to be utterly relevant in determining phase separation and, consequently, charge separation. This is in contrast to the alternating donor:acceptor structure model that simply pictures the co-existence of donor-pure and acceptor-pure phases, which in many cases does not account for the complex "mixing and morphological evolution"in BHJs.

The ternary structure was found in several systems, including the stereotype P3HT:$PC_{61}BM$ samples where such alternative donor:acceptor structure was believed to work best.[52] The thin films were instead found to adopt homogeneous structure with separate P3HT and $PC_{61}BM$ crystalline domains, and amorphous regions in between. Based on the analysis of the Porod scattering regime, going from 20 vol % of fullerene, where the only crystalline phase is composed of P3HT, to 50 vol % fullerene in which fullerene aggregates also showed up, the amorphous phase was always present in the thin films. Annealing to some extent changes the film morphology, although it did not start phase separation in 20 vol % $PC_{61}BM$ sample until after 6 h, while annealing of the 50 vol % $PC_{61}BM$ sample led immediately to interface blurring due to $PC_{61}BM$ crystal growth. The relative high current density despite the amorphous region was shown to be carried out through intermolecular charge transport between neighbouring PCBM molecules.

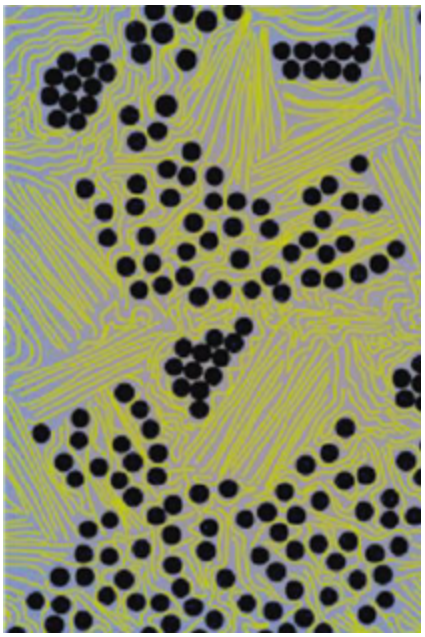

Figure 1.4 Ternary structure of a BHJ blend, it includes the relative crystalline polymer domains, represented by the yellow stacks, the relative crystalline crystalline fullerene domains, represented by the aggregated black dots and the amorphous domains. Taken from ref[52].

Reduction of the blend phase would lead to the deteriorated device performance. Thermal annealing was a great recipe for P3HT:PCBM devices as it increased the crystallinity of the film. However, destruction of percolation pathway upon annealing was found to decrease device performance in the blend of PBDTTPD with PCBM.[51] Device parameters such as V_{oc}, J_{sc}, FF and PCE were all found to decrease after thermal anealing. The degraded performance was also found to be uniform across all the wavelength range being measured. This implies that the origin of this decay in performance lies in the microscopic structure rather than of a single material within the device. By performing GISAXS measurements, the OPV film was divided into three different parts, the polymer-rich regions, the fullerene-rich regions and the blend regions.

Thermal annealing was found to significantly reduce the portion of the blend phase. Thus it was concluded that percolation in the blend phase was damaged after thermal annealing.

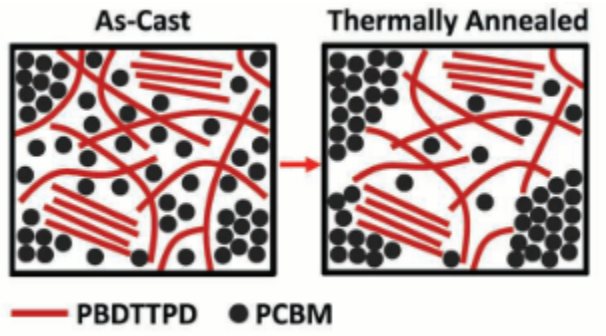

Figure 1.5 Annealing degraded device performance by increasing crystallinity and reducing the amorphous regions, which cut off the percolation pathway of charge carriers. Taken from ref[51].

The amorphous regions could be comprised of intercalated fullerenes into the polymer sidechains. In a recent by Miller *et al.*,[53] it was studied how stereo-chemical modification (branching) of the intercalated fullerenes impacts charge transport. The OPV performance of the polymers P3HT and PBTTT blended with the fullerene derivatives ICMA, ICBA and ICTA was tested. ICMA, ICBA and ICTA are fullerene derivatives with one, two and three adducts, respectively. These fullerene derivatives with different numbers of side chains were shown to affect the performance significantly. When blended with PBTTT, ICMA showed much higher performance than the PBTTT film blended with ICBA or ICTA. Microscopic structure studies based on GISAXS showed that crystal constants in the a-direction did not change in these devices with different fullerenes. This means that although baring a larger molecular volume, ICBA/ICTA molecules were still accommodated inside the cage formed by PBTTT sidechains

and the polymer backbones, in analogy to the better performing ICMA. While this intercalated structure poses little problem for charge transport through ICMA, the highly brached nanostructure of ICBA and ICTA imposes constraints to the electron percolation pathway through the fullerene moiety.

Even in the polymer-only films, structural disorder was shown to be crucial for charge generation and transport. [54]Charge transport was shown to be carried out by the interconnected regions of polymer aggregates, with a feature of the 0-1 peak in the electroluminescence feature. By comparing a large library of polymers with different degrees of structural disorder, it was suggested that energy disorder does not always follow the trend of structural disorder, which is apparently true for the new class of polymer such as PNDI-T2 with relative higher disorder yet higher mobility than traditional material such as P3HT. It was concluded that more structural disorder would be beneficial for the device performance as long as the material does not become amorphous.

Charge separation was confirmed to happen at the interface between ordered and amorphous regions in polymer-only films.[55] Microstructure was found to be essential in controlling the yield and decay dynamics of charge carriers in polymer-only films. Films of P3HT a MW of 5.5-347 kg/mol were investigated. The photogeneration of charges was found to increase with MW until a transition point, after which the free exciton bandwidth and charge decay dynamics were both found to decrease sharply. The transition point, determined via a tensile test, represents the transformation from a non-entangled, paraffin-like state to an entangled, semicrystalline state. These observations allowed to conclude that the energy landscape at the interface between amorphous and crystalline domains of P3HT is essential for both charge generation and recombination.

While the process of charge generation highlights the importance of amorphous regions, the crystalline domains are crucial for charge separation. In the PBTTT:PCBM blend, a higher efficiency in OPV device performance was correlated with the formation of PCBM crystallites, corroborated through calorimetric characterization.[49] Cyclic-voltammetry measurements indicate that larger PCBM crystallites possess higher electron affinity. Photoluminescence efficiency also decreased in the blend with larger PCBM crystallites. It was thus suggested that the PCBM crystallites serve as electron sink for charges generated at the interface. Similar results have been found for the donor material.

This disordered structure is also supported by Monte Carlo simulation. In a paper by McMahon *et al.*,[56] it was argued that crystallization of polymer and fullerene would leave out free volume for the mixed domain where significant energy disorder could happen, thus contributing to an energy gradient at the interface. This energy gradient at the interface would make geminate pair dissociation less field dependent. However, the Monte Carlo simulations also showed that for this energy gradient to be effective, the interface holding the energy gradient should be very thin, ~1 nm, making it difficult to control.[57] This model also pointed out that energy disorder in the bulk would facilitate geminate dissociation, which supports the ternary phase picture by proposing the cascaded energy levels at the donor:acceptor interface accelerate charge dissociation.

Notably, ultrafast charge separation at the donor:acceptor interface has been explained by the relaxation through the density of states within each material in this model.[21] Larger energy disorder was found to lead to more efficient charge separation. With disorder of 0.10 eV and 0.12 eV for PCBM and MDMO-PPV, respectively, 75% separation yield was predicted with an energy loss of ~0.1 eV.

1.4 Delocalization

Ultrafast charge separation could also be explained by charge delocalization. In the dynamic Monte Carlo simulation performed by Deibel *et al*.,[50] the efficient polaron-pair dissociation was solved by assuming charge delocalization on the polymer backbone. The resulting larger charge carrier mobility together with the smaller Coulombic attraction due to the increased polaron-pair radius could separate the polaron with a yield of 90% at 10^7 V/m when conjugation length was 10 units for P3HT.

The efficiency of OPV devices would have been poor provided all the thin films are totally amorphous. Delocalization of charge carrier simply provides an alternative to the explanation of the picture, in agreement with many structural and spectral observations. Not only could the ultrafast charge separation could be expected. Effective mass of electron is also reduced by delocalization. Braun-Onsager model taking into account of the effective mass of electron could also explain the ultrafast charge separation.[47]

Delocalization could reduce excess energy for charge separation. There are doubts regarding whether as much excess energy as 0.6 eV is needed for charge separation. This question was addressed based discussion on the dynamics of charge species following a series of optical spectroscopy pump-probe experiments.[58] Charge delocalization rather than relaxation in the density of state was proposed to be the mechanism for ultrafast charge separation. When the below-gap push beam was applied to excite vibronically relaxed states picoseconds after the above-gap pump beam, different blend systems demonstrated different degree of increase in photocurrent, where most dramatic change happens in the inefficient blend of PFB:F8BT and the

least change in the efficient system of PCPDTBT:PCBM. The percentage increase of photocurrent after push beam after excitation with above-gap and below-gap energies together is similar, indicating that the nature of CT states obtained after the initial pump beam is similar. This suggests that hot CT states are vital in producing photocurrent. By comparing with QC calculations, it was proposed that CT delocalizaton is important for efficient charge separation. Energy disorder thus is not required in the delocalization model as in the case of relaxation in DOS. Energy loss of above gap excitation is believed to be unnecessary loss, a result of our inability to produce more crystalline structures, rather than playing a key role ensuring charge separation.

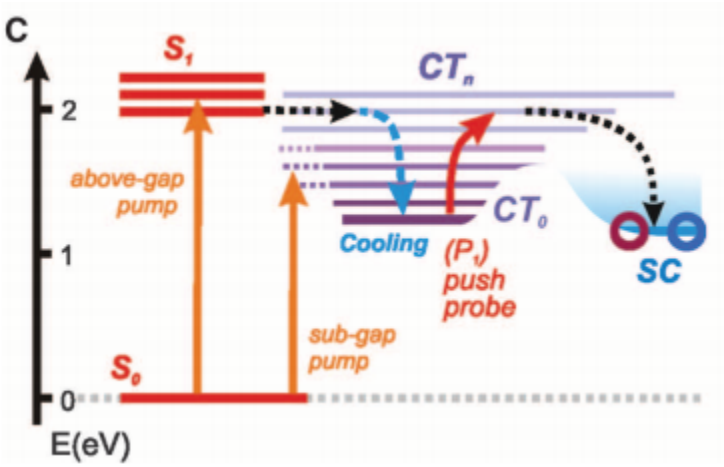

Figure 1.6 Schematics on the function of pump-push in exciting cooled CT states. Charge separation could either be achived through one-step excitation from S_0 to S_n states and following relaxation within the charge transfer manifolds (CT) until charge separation. Or it could be achieved by firstly excitation to lower lying CT states and move towards charge separation with the extra push energy from another photon. Taken from ref[58].

In many systems where ultrafast charge separations were observed, energy disorder in the film was found to reduce device performance through enhanced bimolecular recombination. In the blend of PCPDTBT:PCBM, when there were no 1,8-octanedithio (DIO) additives, morphology remained amorphous and charge separation was found to happen in less than 100 fs.[7] However, in the case where DIO additives were applied, morphology became more crystalline and energy disorder being reduced, device performance improved by a factor of 2 and charge separation becomes limited by diffusion to the grain boundaries, even there was not much improvement on charge separation rate. Similar results have been shown for regioregular P3HT:PCBM blend with and without thermal annealing,[59] where better device performance was correlated with larger crystalline domains as a result of thermal annealing. Only the boundaries slowed down charge separation by limiting diffusion of excitons. In the case of regiorandom versus regioregular P3HT blended with PCBM, ultrafast charge separation was found in both films as well, although regioregular P3HT apparently had the more superior performance.[60] Since charge generation is not the bottleneck, in all these case studies the stark difference in device performance was thus attributed to the charge collection process in these films prepared with the same materials but different procedures.

More supportive results of delocalization are from the broadband and wide time scale measurements, which characterized a wide range of charge species across orders of magnitude time scale to reveal the dynamics of different species. The results implied that relaxation of exciton in its DOS would not contribute to photocurrent, but carrier relaxing would lead to trap states which led to more non-geminate recombination.[61] In this work by Etzold *et al.*, 500 – 1100 nm broadband transient absorption spectroscopy was used to probe time range between 2 ns and

1 ms. It was found that 11% of the initial CT states being generated ended up geminately recombined, and the emission from these states redshifted. The other 89% of the charges created on the ultrafast time scale contributed to photocurrent, and they contributed to ground states bleaching. This supported the idea that delocalized exciton, rather than the relaxed 11% through energy disorder, led to better charge separation. As PCDTBT:PCBM blend appear amorphous, yet a high degree of the excitons generated ended up delocalized, the implication is that delocalization may not require crystalline structure on the 100 nm scale. Avoiding overwhelming molecularly intermixing and increase crystallinity on the sub-100 nm should be desirable.

Exciton delocalization was also shown to reduce the recombination rate. Recombination rates of exciton states would have been devastating for performance of OPV efficiency provided every formation of an exciton lead to charge annihilation at the $10^{16} \sim 10^{17}$ cm^{-3} charge density. Rao *et al.* recently demonstrated that in the blends with 1:3 ratio of PIDT:PhanQ with C_{60} based fullerene of PCBM, ICMA and ICBA,[27] triplet states only showed up in the photoinduced spectrum with ICMA and ICBA, while the triplet species demonstrated diffusion limited transport character according to their fluence and temperature dependence. Triplet feature appear in the PCBM blend only when the polymer:fullerene ratio is raised to 1:1. Combined with the larger fullerene aggregated structures observed in neutron scattering data, the authors conclude that the higher performance in the 1:3 blend of PIDT:PhanQ with PCBM is due to the reduced recombination as a result of the faster regeneration of CT states from the delocalized triplet states.

1.5 Ways to Understand Morphology Formation

The dependence of device performance on morphology appears more intangible due to our inability to control the morphology. Often happening in the research is with the advent of a new material more than one parameter has changed. It is thus less valid to expand the morphology model as a standard. Ways to understand the morphology formation process have been studies in a few cases.

Film structure could be described by Clory-Huggins model, which predicts the miscibility of two materials. Gomez *et al.* found at φ_{PCBM} >0.58 passing the miscibility point, larger aggregates of PCBM was found concurrent with the leap of electron mobility.[62]

Hanson Solubility Parameters (HSP) evaluate the dispersion forces, dipole interactions and hydrogen bondings of a material in a range of solvent.[63] It wa applied successfully to explain the aggregation in thin films from different solvents. Addition of 2 vol % to P3HT solution in chloroform was found to increase the supramolecular assembly. As a result, the field effect mobility was found to increase by 4 folds. The increased aggregation was attributed to the slower evaporation of mixed solvents and also the lower solubility of P3HT within. It was found the RED value, an estimate of the miscibility of two materials, of P3HT increased increased to one during film formation, indicating that aggregation was a result of the unfavorable solvent-solute interaction.

The application of HSP was also explored in the formation of bulk heterojunctions. Duong *et al.* examined HSP in a series of polymers,[64] small molecules and fullerene derivatives combinations in 27 solvent systems. Size of the aggregate was measured in tapping-mode AFM and analyzed with power spectrum density, 2D Fourier Transform, grain size calculation and trace cross section. MDMO-PPV:$PC_{61}BM$ and MEH-PPV: $PC_{61}BM$ films shared similar HSP

values and optical properties, yet the former film is full of bubble-like features which were absent in the latter. This difference was postulated to origin from fullerene can more easily intercalate into the free space between alkyl chains in MDMO-PPV. Moreover, HSP in the liquid phase was applied to BHJ systems where $PC_{61}BM$ was considered as the solid solvent. Quite contrary to the assumption that those more soluble materials in $PC_{61}BM$ should form smaller phase separation, small molecules $DPP(PhTT)_2$ films form finer structures with $PC_{61}BM$ $DPP(TBFu)_2$ although it is more soluble inside. The role of spin-coating speed was also examined and it was suggested that faster evaporation time left less time for aggregate formation and thus resulted in finer structures. It was suggested that morphology is a convolution of the solubility, evaporating rate and cohesive energy.

Time-resolved observations were made on polymer systems during spin-coating.[65] Combination of in-situ quartz crystal microbalance measurements with dissipation capabilities and in-situ grazing incidence wide-angle X-ray scattering in an environmental controlled chamber could distinguish the onset of nucleation. By comparing with optical microscopy and AFM topography, slower evaporation was found to result in more surface-covering large platelet-like domains, while faster evaporation ended up with fewer isolated platelet-like domains. These observations support the idea that slower evaporation of solvent predominantly initiated nucleation at the liquid-substrate interface. This is turn might help understand film formation.

New models taking into account of the electronic interactions might better explain the film formation. Study of the polymer physics could more insight towards controlling the morphology in polymer thin films. One example could be the gelation of polymer solution. Gelation in polymer physics could be related to the packing number of polymer chains. By plotting the

gelation concentration of polymer at different temperature, Eldridge-Ferry plot will allow us to find the statistical average of cross-linking regions,[66] which is essentially the pacing region of polymer, by studying the slope, ln(c) vs. 1/T slope.

$$\ln(c) = \Delta H_0/k_BT + \text{const.} \qquad \text{Equation 1.1}$$

The enthalphy ΔH_0 is expected to be the proportional to the number of segments participating in the junction. One would also expect ΔH_0 to be proportional to segment size. By correlating this H_0 value to the crystal constants obtained in X-ray scattering or other techniques, more information on the packing density happens during film formation could be inferred, such as molecular weight dependence and disorder dependence.

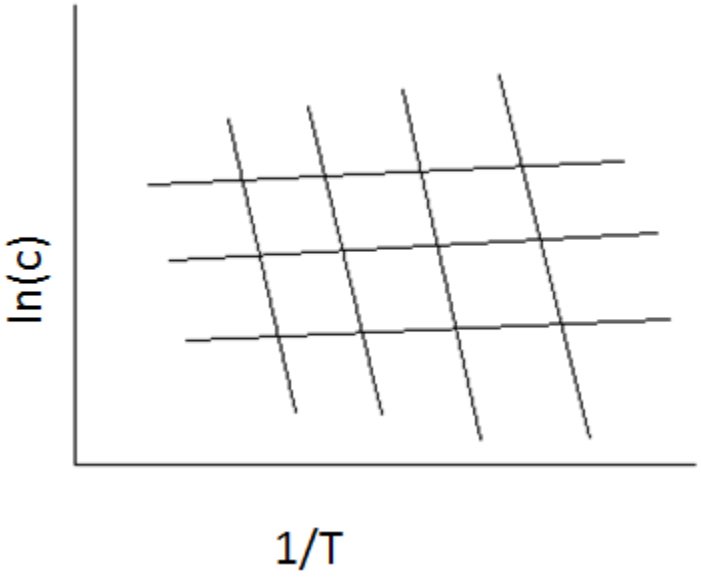

Figure 1.7 Eldridge-Ferry plot, polymer packing in solution transfer into different packing density in thin films

1.6 Conclusion

A real OPV device is comprised of structures across a wide spatial range from sub nm to μm. Molecular stacking determined by side chain, backbone rigidity affects the interchain transport. Crystalline structure on the 1~10 nm scale is ideal for majority carrier transport, slowed only by the grain boundaries. Phase separation at an even larger length scale, ~100 nm or more, affect exciton dissociation and charge transport.

We reviewed recent developments in understanding of the microscopic structure of OPV devices, how understanding of the microstructure in different contexts led to different understanding on the morphology performance relationship. People from different background such as X-ray scattering and optical spectroscopy hold different opinions on the role of crystallinity. While the former observed the molecularly intermixing and realizes the importance of a distribution of structural features, the latter group based on the dynamics of active optical species suggests that more energy than needed is lost on the disordered regions. There is no widespread agreement on what should be the optimal phase separation in size and purity. In this delicate balance, too small phase separation would lead to CT states that could not be separated thus contribute to geminate recombination. Too large separation on the other end would not provide adequate percolation pathway for charge transport, which in turn increased bimolecular recombination. Part of this confusion comes from our lack of ability to characterize and understand the all the important aspects of morphology simultaneously. Most observations to

date regarding to the interaction between structure and property are based on the ensemble averaging. It describes the device behavior as a whole, without much reference to local charge carrier dynamics. While advantageous in capturing the general trend in relating energy levels to device performance, it is also likely to miss out optoelectronic information on the microscopic scale. New characterizing techniques should be able to further help us understand the effect of microstructure on charge generation.[67, 68]

Larger dielectric constant would reduce the chances for charges to recombine. However, material design schemes with higher planarity and higher structural disorder have both been suggested to lead towards a higher PCE, leaving us with the opportunities to explore the role the morphology in OPV operation. Further study of the microstructure and photophysics of OPV device would surely lead to better understanding and potentially better control of film morphology.

1.7 References

1. J. Y. Kim, K. Lee, N. E. Coates, D. Moses, T. Q. Nguyen, M. Dante and A. J. Heeger, *Science*, 2007, **317**, 222-225.
2. W. W. Li, A. Furlan, K. H. Hendriks, M. M. Wienk and R. A. J. Janssen, *Journal of the American Chemical Society*, 2013, **135**, 5529-5532.
3. L. T. Dou, J. B. You, J. Yang, C. C. Chen, Y. J. He, S. Murase, T. Moriarty, K. Emery, G. Li and Y. Yang, *Nature Photonics*, 2012, **6**, 180-185.
4. W. U. Huynh, J. J. Dittmer and A. P. Alivisatos, *Science*, 2002, **295**, 2425-2427.

5. Z. M. Beiley and M. D. McGehee, *Energy & Environmental Science*, 2012, **5**, 9173-9179.

6. X. L. Liu, S. Huettner, Z. X. Rong, M. Sommer and R. H. Friend, *Advanced Materials*, 2012, **24**, 669-+.

7. F. Etzold, I. A. Howard, N. Forler, D. M. Cho, M. Meister, H. Mangold, J. Shu, M. R. Hansen, K. Muellen and F. Laquai, *Journal of the American Chemical Society*, 2012, **134**, 10569-10583.

8. T. M. Clarke, A. M. Ballantyne, J. Nelson, D. D. C. Bradley and J. R. Durrant, *Advanced Functional Materials*, 2008, **18**, 4029-4035.

9. G. Li, Y. Yao, H. Yang, V. Shrotriya, G. Yang and Y. Yang, *Advanced Functional Materials*, 2007, **17**, 1636-1644.

10. Z. C. He, C. M. Zhong, S. J. Su, M. Xu, H. B. Wu and Y. Cao, *Nature Photonics*, 2012, **6**, 591-595.

11. M. A. Green, K. Emery, Y. Hishikawa, W. Warta and E. D. Dunlop, *Prog Photovoltaics*, 2013, **21**, 1-11.

12. X. Xiao, G. D. Wei, S. Y. Wang, J. D. Zimmerman, C. K. Renshaw, M. E. Thompson and S. R. Forrest, *Advanced Materials*, 2012, **24**, 1956-1960.

13. Y. Zhang, J. Y. Zou, H. L. Yip, K. S. Chen, D. F. Zeigler, Y. Sun and A. K. Y. Jen, *Chemistry of Materials*, 2011, **23**, 2289-2291.

14. M. C. Scharber, D. Wuhlbacher, M. Koppe, P. Denk, C. Waldauf, A. J. Heeger and C. L. Brabec, *Advanced Materials*, 2006, **18**, 789-+.

15. M. M. Lee, J. Teuscher, T. Miyasaka, T. N. Murakami and H. J. Snaith, *Science*, 2012, **338**, 643-647.

16. Y. M. Sun, G. C. Welch, W. L. Leong, C. J. Takacs, G. C. Bazan and A. J. Heeger, *Nature Materials*, 2012, **11**, 44-48.

17. N. C. Giebink, G. P. Wiederrecht, M. R. Wasielewski and S. R. Forrest, *Physical Review B*, 2011, **83**, 195326-195321-195326.

18. K. Vandewal, K. Tvingstedt, A. Gadisa, O. Inganas and J. V. Manca, *Nature Materials*, 2009, **8**, 904-909.

19. J. D. Zimmerman, X. Xiao, C. K. Renshaw, S. Y. Wang, V. V. Diev, M. E. Thompson and S. R. Forrest, *Nano Letters*, 2012, **12**, 4366-4371.

20. Y. T. Fu, C. Risko and J. L. Bredas, *Advanced Materials*, 2013, **25**, 878-882.

21. H. van Eersel, R. A. J. Janssen and M. Kemerink, *Advanced Functional Materials*, 2012, **22**, 2700-2708.

22. L. J. A. Koster, S. E. Shaheen and J. C. Hummelen, *Advanced Energy Materials*, 2012, **2**, 1246-1253.

23. D. Di Nuzzo, G.-J. A. H. Wetzelaer, R. K. M. Bouwer, V. S. Gevaerts, S. C. J. Meskers, J. C. Hummelen, P. W. M. Blom and R. A. J. Janssen, *Advanced Energy Materials*, 2013, **3**, 85-94.

24. D. Veldman, S. C. J. Meskers and R. A. J. Janssen, *Advanced Functional Materials*, 2009, **19**, 1939-1948.

25. T. M. Clarke and J. R. Durrant, *Chemical Reviews*, 2010, **110**, 6736-6767.

26. J. Rivnay, S. C. B. Mannsfeld, C. E. Miller, A. Salleo and M. F. Toney, *Chemical Reviews*, 2012, **112**, 5488-5519.

27. A. Rao, P. C. Y. Chow, S. Gelinas, C. W. Schlenker, C. Z. Li, H. L. Yip, A. K. Y. Jen, D. S. Ginger and R. H. Friend, *Nature*, 2013, **500**, 435-+.

28. C. J. Brabec, G. Zerza, G. Cerullo, S. De Silvestri, S. Luzzati, J. C. Hummelen and S. Sariciftci, *Chemical Physics Letters*, 2001, **340**, 232-236.

29. R. R. Lunt, N. C. Giebink, A. A. Belak, J. B. Benziger and S. R. Forrest, *Journal of Applied Physics*, 2009, **105**.

30. D. Caruso and A. Troisi, *Proceedings of the National Academy of Sciences of the United States of America*, 2012, **109**, 13498-13502.

31. F. Paquin, G. Latini, M. Sakowicz, P. L. Karsenti, L. J. Wang, D. Beljonne, N. Stingelin and C. Silva, *Physical Review Letters*, 2011, **106**.

32. A. C. Morteani, P. Sreearunothai, L. M. Herz, R. H. Friend and C. Silva, *Physical Review Letters*, 2004, **92**.

33. H. Imahori, K. Tamaki, D. M. Guldi, C. P. Luo, M. Fujitsuka, O. Ito, Y. Sakata and S. Fukuzumi, *Journal of the American Chemical Society*, 2001, **123**, 2607-2617.

34. D. C. Coffey, B. W. Larson, A. W. Hains, J. B. Whitaker, N. Kopidakis, O. V. Boltalina, S. H. Strauss and G. Rumbles, *Journal of Physical Chemistry C*, 2012, **116**, 8916-8923.

35. C. W. Schlenker and M. E. Thompson, *Chem Commun*, 2011, **47**, 3702-3716.

36. G. Li, V. Shrotriya, J. S. Huang, Y. Yao, T. Moriarty, K. Emery and Y. Yang, *Nature Materials*, 2005, **4**, 864-868.

37. O. Inganas, F. L. Zhang, K. Tvingstedt, L. M. Andersson, S. Hellstrom and M. R. Andersson, *Advanced Materials*, 2010, **22**, E100-E116.

38. M. M. Wienk, J. M. Kroon, W. J. H. Verhees, J. Knol, J. C. Hummelen, P. A. van Hal and R. A. J. Janssen, *Angew Chem Int Edit*, 2003, **42**, 3371-3375.

39. H. Y. Chen, J. H. Hou, S. Q. Zhang, Y. Y. Liang, G. W. Yang, Y. Yang, L. P. Yu, Y. Wu and G. Li, *Nature Photonics*, 2009, **3**, 649-653.

40. S. H. Park, A. Roy, S. Beaupre, S. Cho, N. Coates, J. S. Moon, D. Moses, M. Leclerc, K. Lee and A. J. Heeger, *Nature Photonics*, 2009, **3**, 297-U295.

41. B. C. Thompson and J. M. J. Frechet, *Angew Chem Int Edit*, 2008, **47**, 58-77.

42. G. Q. Ren, C. W. Schlenker, E. Ahmed, S. Subramaniyan, S. Olthof, A. Kahn, D. S. Ginger and S. A. Jenekhe, *Advanced Functional Materials*, 2013, **23**, 1238-1249.

43. C. W. Schlenker, K.-S. Chen, H.-L. Yip, C.-Z. Li, L. R. Bradshaw, S. T. Ochsenbein, F. Ding, X. S. Li, D. R. Gamelin, A. K. Y. Jen and D. S. Ginger, *Journal of the American Chemical Society*, 2012, **134**, 19661-19668.

44. D. Di Nuzzo, A. Aguirre, M. Shahid, V. S. Gevaerts, S. C. J. Meskers and R. A. J. Janssen, *Advanced Materials*, 2010, **22**, 4321-+.

45. L. Onsager, *Phys Rev*, 1938, **54**, 554-557.

46. A. Tada, Y. F. Geng, Q. S. Wei, K. Hashimoto and K. Tajima, *Nature Materials*, 2011, **10**, 450-455.

47. C. Schwarz, S. Tscheuschner, J. Frisch, S. Winkler, N. Koch, H. Bassler and A. Kohler, *Physical Review B*, 2013, **87**.

48. Y. B. Yuan, T. J. Reece, P. Sharma, S. Poddar, S. Ducharme, A. Gruverman, Y. Yang and J. S. Huang, *Nature Materials*, 2011, **10**, 296-302.

49. F. C. Jamieson, E. B. Domingo, T. McCarthy-Ward, M. Heeney, N. Stingelin and J. R. Durrant, *Chemical Science*, 2012, **3**, 485-492.

50. C. Deibel, T. Strobel and V. Dyakonov, *Physical Review Letters*, 2009, **103**.

51. J. A. Bartelt, Z. M. Beiley, E. T. Hoke, W. R. Mateker, J. D. Douglas, B. A. Collins, J. R. Tumbleston, K. R. Graham, A. Amassian, H. Ade, J. M. J. Frechet, M. F. Toney and M. D. McGehee, *Advanced Energy Materials*, 2013, **3**, 364-374.

52. W. Yin and M. Dadmun, *Acs Nano*, 2011, **5**, 4756-4768.

53. N. C. Miller, S. Sweetnam, E. T. Hoke, R. Gysel, C. E. Miller, J. A. Bartelt, X. X. Xie, M. F. Toney and M. D. McGehee, *Nano Letters*, 2012, **12**, 1566-1570.

54. R. Noriega, J. Rivnay, K. Vandewal, F. Koch, N. Stingelin, P. Smith, M. Toney and A. & Salleo, *Nature Materials*, 2013, **ASAP**.

55. O. G. Reid, J. A. N. Malik, G. Latini, S. Dayal, N. Kopidakis, C. Silva, N. Stingelin and G. Rumbles, *J Polym Sci Pol Phys*, 2012, **50**, 27-37.

56. D. P. McMahon, D. L. Cheung and A. Troisi, *Journal of Physical Chemistry Letters*, 2011, **2**, 2737-2741.

57. C. Groves, *Energy & Environmental Science*, 2013, **6**, 1546-1551.

58. A. A. Bakulin, A. Rao, V. G. Pavelyev, P. H. M. van Loosdrecht, M. S. Pshenichnikov, D. Niedzialek, J. Cornil, D. Beljonne and R. H. Friend, *Science*, 2012, **335**, 1340-1344.

59. R. A. Marsh, J. M. Hodgkiss, S. Albert-Seifried and R. H. Friend, *Nano Letters*, 2010, **10**, 923-930.

60. J. Guo, H. Ohkita, H. Benten and S. Ito, *Journal of the American Chemical Society*, 2010, **132**, 6154-6164.

61. F. Etzold, I. A. Howard, R. Mauer, M. Meister, T.-D. Kim, K.-S. Lee, N. S. Baek and F. Laquai, *Journal of the American Chemical Society*, 2011, **133**, 9469-9479.

62. K. Vakhshouri, D. R. Kozub, C. Wang, A. Salleo and E. D. Gomez, American Physical Society, Physical Review Letters, 2012, vol. 108, p. 026601.

63. M. Chang, D. Choi, B. Fu and E. Reichmanis, *Acs Nano*, 2013, **7**, 5402.

64. D. T. Duong, B. Walker, J. Lin, C. Kim, J. Love, B. Purushothaman, J. E. Anthony and T. Q. Nguyen, *J Polym Sci Pol Phys*, 2012, **50**, 1405-1413.

65. R. P. Li, H. U. Khan, M. M. Payne, D. M. Smilgies, J. E. Anthony and A. Amassian, *Advanced Functional Materials*, 2013, **23**, 291-297.

66. F. Tanaka, *Polymer Physics : Applications to Molecular Association and Thermoreversible Gelation*.

67. D. C. Coffey and D. S. Ginger, *Nat Mater*, 2006, **5**, 735-740.

68. B. A. Collins, J. E. Cochran, H. Yan, E. Gann, C. Hub, R. Fink, C. Wang, T. Schuettfort, C. R. McNeill, M. L. Chabinyc and H. Ade, *Nature Materials*, 2012, **11**, 536-543.

Chapter 2

Morphology Dependent Trap Formation in Bulk Heterojunction Photodiodes

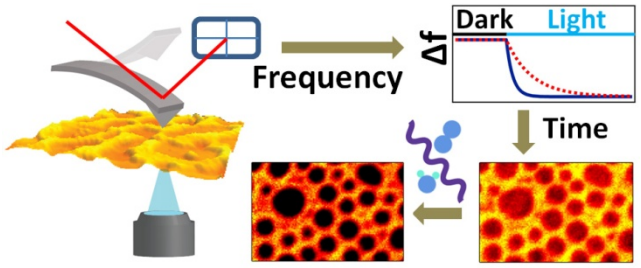

2.1 Introduction

Since the first reports of blended polymer heterojunctions,[6540, 5243] the efficiency of organic photovoltaics has improved dramatically, with reports of single layer devices now approaching 10% and tandem organic solar cells exceeding 10%. Over the same time period, scientific interest in these materials has also increased—in part because of the potential to achieve large area, low cost solar cells via solution processing of flexible organic semiconductors.[23, 3, 30, 5] Nevertheless, a major concern that could limit the widespread use of organic photovoltaics (OPV) is their long term stability.[7]

Studies have shown that OPV device performance tends to degrade over time because of several causes,[7, 20] including chemical interactions at the metal/organic interface,[7] morphological

instabilities in the blended active layers,[6] and both reversible and irreversible chemical changes of the semiconductor materials.[6] To some extent, inverted device architectures have mitigated the need for reactive metal cathodes,[14-15, 25] and a variety of cross-linking and other strategies can be used to stabilize polymer film morphologies.[48, 21, 14] On the other hand, suppressing chemical changes in the organic semiconductors is still largely achieved via encapsulation.[7]

Even if organic photovoltaics ultimately use some form of encapsulation, a better fundamental understanding of the mechanisms that lead to chemical degradation of active organic semiconductor layers in bulk heterojunction OPVs could still enable better design, synthesis, and processing strategies to achieve more stable OPV devices. While there has been a limited amount of work in this area,[7, 20, 8] the correlations between local film structure and photooxidation/trap formation in organic photovoltaics are essentially unknown. This is unfortunate, as heterogeneity is ubiquitous in organic semiconductors,[5, 6, 20] and one might expect local compositional or structural variations to lead to variations in degradation rates.

Photooxidation of OPVs is often studied by optical methods,[7, 46, 19] which yield chemical specificity but lack electrical information. Furthermore, optical probes are typically diffraction-limited with resolutions of hundreds of nanometers.[46, 19] On the other hand, electrical scanning probe microscopy methods have the potential to probe local variations in OPV properties such as charge transport, photocurrent collection, and trapping/recombination.[3, 1, 7, 48, 7, 7] Indeed, we have previously shown that time-resolved electrostatic force microscopy (trEFM) can be used to characterize local trap formation in conjugated polymer blends.[48] However, in that work we did not study the spatial variations in photooxidation across a heterogeneous film. Likewise, Sengupta et al. have applied cAFM and SKPM to study photooxidation of polymer blends,[40] but focused their studies only on differences between light and dark exposed regions of an OPV

film—and not on variations in photooxidation across the structurally heterogeneous domains of the BHJ film.

Here, we bridge this critical gap to demonstrate that local composition affects the rate of photooxidation in nanostructured polymer solar cells. We do so by comparing trEFM with conventional device measurements on blends of the model polymers poly(9,9'-dioctylfluorene-*co*-bis-*N,N'*-(4-butylphenyl)-bis-*N,N'*-phenyl-1,4-phenylene-diamine) (PFB), and poly(9,9'-dioctylfluorene-*co*-benzothiadiazole) (F8BT).

2.2 Materials and Methods

Materials and device fabrication. PFB (MW=80,000-120,000, PDI=2.0) was purchased from American Dye Source (ADS232GE). F8BT (MW=10,000-20,000, PDI<3) was purchased from Sigma-Aldrich (product #698687). Structures for both materials are shown in Fig. 1. Xylene solvent was purchased from Sigma-Aldrich (product #214736), degased and dried with 4 Angstrom molecular sieves before use. 1:1 weight ratio PFB:F8BT solutions were made from mixing 20 mg/mL of PFB in xylenes solution and 20 mg/mL F8BT in xylenes solution. To form devices, 90 nm of PEDOT:PSS (HC Stark PEDOT 4083, LOT# LVW950) was spincoated onto an ITO substrate (Thin Film Devices, OLED/solar applications) and annealed at 120°C under N_2 atmosphere for 1 h. The PFB:F8BT solution was then spincoated onto the PEDOT: PSS covered ITO in N_2 glovebox to form an 80 nm active layer. For trEFM, the film was then loaded into a flow cell with a 150 cc/min dry N_2 flow.

Photooxidation. After the PFB:F8BT blend films were made, a UV-vis spectrum was taken on one of the films to extract the absorption at each of the three degrading wavelengths of trEFM. Then the films were exposed without top electrodes to different wavelengths, making the

absorbed photon dose to be 6.0×10^{10} photons/μm^2, equal to that used in the trEFM measurements; for the *in situ* experiments, see below. The PFB:F8BT films were then loaded into an evaporator and 60 nm thick Al top electrodes were deposited at 0.1 nm/s with a base pressure of 1.2×10^{-6} mbar in an Edwards 306 AUTO evaporator. EQE measurements were performed under vacuum with light from a halogen lamp dispersed by a Spectra Pro 2150i monochromator from Acton Research Corporation.

GATR-FTIR. The degradation procedures were the same as for devices. Measurements were carried out on a Nicolet 8700 FT-IR spectrometer (Thermo Scientific) equipped with a HgCdTe detector, GATR grazing angle ATR accessory (Harrick Scientific) with a 65° fixed incident angle and a 56 in-oz slip clutch. The spectrometer and accessory were purged with dry N_2 gas. Each spectrum was taken with 256 averages. Each raw spectrum was corrected with atmospheric suppression and ATR correction, the baseline was then subtracted.

AFM. trEFM measurements were carried out on MFP-3D-BIO (Asylum Research) based AFM with custom modifications using 300 kHz Pt-coated cantilevers (BudgetSensor ElectriTap300). trEFM was carried out in a flow cell, at a lift height of 10 nm. For all the trEFM data, the flow cell was connected to flowing nitrogen. The flow cell used here has a 1.50-2.55 mL fluid volume after engaging the tip. For photooxidation, the flow cell was connected to compressed air and exposed to light calibrated to yield an absorbed photon dose of $6.0\times10^{10}/\mu m^2$. The system was then purged again with nitrogen for another 20 min before taking the post-oxidation trEFM images. The trEFM setup used is shown in Fig. 2 and is described in detail elsewhere. [9, 2] The 365 nm, 405 nm and 455 nm LEDs were purchased from LED Engin (product numbers LZ1-00U600, LZ1-00UA00, LZ1-00DB00, respectively). Incident illumination power was calibrated

using a Si diode and film absorbance spectra to ensure a constant absorbed photon dose at each wavelength.

2.3 Results and Discussion

For these experiments we chose the well-characterized model polyfluorene copolymer blend PFB:F8BT because this system provides a morphology that can be easily tailored by casting from different solvents,[17, 12] and because the composition of the resulting structures have been well characterized by a range of experimental methods.[14, 39, 9]

Fig. 1 shows the structures, absorption spectra, and energy levels[47, 20] of PFB and F8BT, as well as the optical properties of a 1:1 blend cast from xylenes. The absorbance spectra of both materials are consistent with those of classic PFB/F8BT studies,[17, 12] with PFB absorbing most strongly at ~380 nm, and F8BT absorbing most strongly at ~470 nm. To first order, the blend absorption appears primarily as a superposition of the two component peaks, with each material contributing roughly the same optical density at ~405 nm. The different absorption peaks of the two materials prove useful below as it allows us to preferentially excite each material.

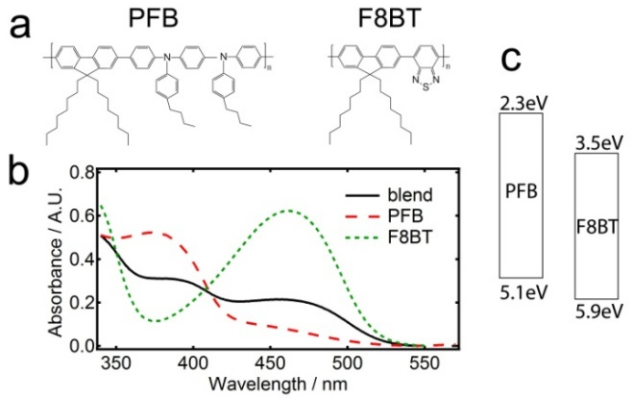

Figure 2.1 (a) Chemical structures of PFB and F8BT. (b) UV-vis absorbance spectra for our PFB, F8BT and 1:1 blend films. (c) HOMO and LUMO levels of PFB and F8BT taken from literature.[47, 20]

Fig. 2 shows a photoluminescence image of a PFB:F8BT blend film excited at 470 nm, collected with an emission filter centered at 530 nm (inset is the topography of the PFB:F8BT blend from an AFM measurement). At 530 nm, the blend emission comes predominantly from the F8BT,[17, 12] and we thus attribute the bright regions in the PL image (higher topography regions in the AFM image) to be F8BT-rich domains, in good agreement with previous reports of PFB/F8BT blends cast from xylenes.[17] The large phase separation is due to the low boiling point of the xylenes solvent being used. Such a coarse ~500 nm scale morphology is not optimal for photodiode performance, but is very useful for unambiguous assignment of the domain composition and facilitates our studies of the differences in stability between different domains. Scanning-transmission x-ray microscopy (STXM) studies of similar compositions of this type of film have shown that the PFB-rich domains are ~70% PFB while F8BT-rich domains are ~90% F8BT.[9]

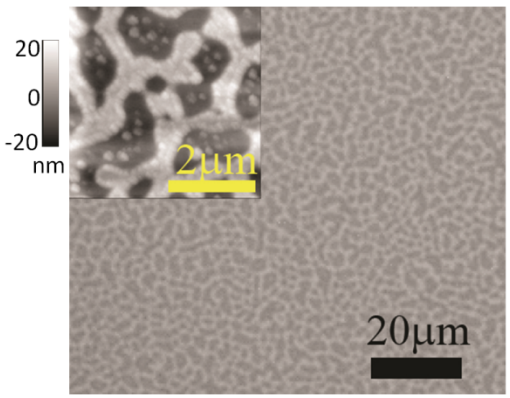

Figure 2.2 Photoluminescence image of a 1:1 PFB:F8BT blend. Excitation at 470nm, emission filtered at 530nm. Inset is the AFM topography of the same film. AFM z-scale bar is shown on the left.

We observe virtually no change in absorbance of the blend before and after photooxidation with 6.0×10^{10} photons/ μm^2 at 405 nm (or 2.9 J/cm^2), as shown in Fig. 3.

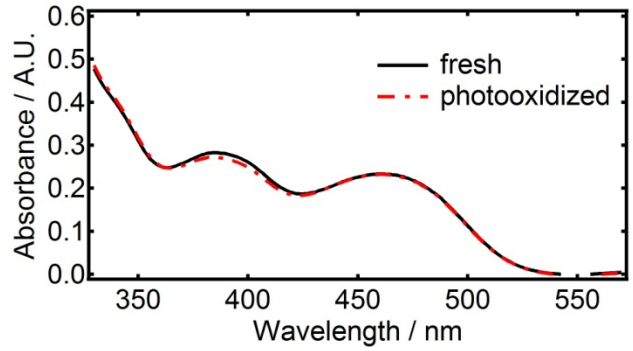

Figure 2.3 UV-vis spectrum of PFB:F8BT blend before (black solid line) and after (red dashed line) photooxidation with 6.0×10^{10} photons absorbed per μm^2.

Fig. 4a shows the external quantum efficiency (EQE) spectrum from a pristine device made from a 1:1 PFB:F8BT film of 80 nm thickness with 60 nm Al top contacts as a black trace. As

expected, the PFB:F8BT combination is rather inefficient,[17, 12] with a peak EQE between 2-3% when processed under these conditions. The pristine blend EQE trace shows features associated with the absorption spectra of both the PFB (shoulder at 405 nm) and F8BT (shoulder at 500 nm) components. Fig. 4a also shows the EQE spectra from identical devices prepared on films that have been degraded in air under 405 nm illumination with absorbed photon dose of $6.0\times10^{10}/\mu m^2$. Importantly, the shoulder of the EQE curve beyond 450 nm (where F8BT dominates the blend absorption) degrades faster than the rest of the EQE curve, regardless of the illumination wavelength being used. Fig. 4b shows this trend more clearly by plotting the ratio of device EQE before and after photooxidation. We note that after photoxidation the photocurrent response over the region from 450-550 nm has degraded more on a relative basis than the photocurrent response over the spectral range from 350-400 nm. Evidently the contribution of F8BT to the overall photocurrent decreases faster than the contribution from PFB for these samples.

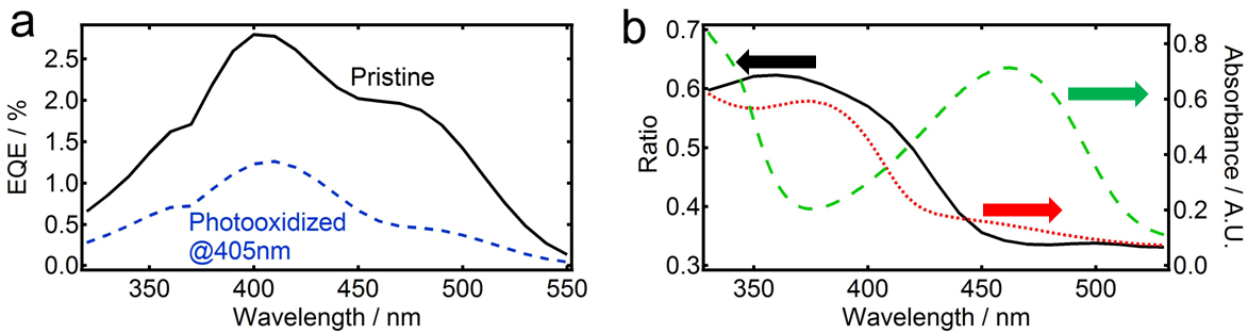

Figure 2.4 (a) EQE spectra of pristine and photooxidized samples. Black solid line is for pristine film. Blue dashed line is for 405 nm photooxidation. (b) The ratio of EQE *vs.* wavelength post/pre photooxidation (black line), plotted on the left axis. Overlaid are the absorbance of PFB

(red dotted line) and F8BT (green dashed line), respectively, plotted for reference on the right axis.

We note that at these photon doses and exposure conditions the decrease in EQE cannot be from bleaching of the polymer absorption as there is no significant change in the UV-Vis spectrum of the blend, as shown in Fig. 3. Furthermore, there is little change even in the photoluminescence spectrum or intensity of the blend (see Fig. 5). Thus the loss in photocurrent is likely due to local trap formation which changes the recombination/transport balance in the film so that even though absorption of photons is not significantly altered, the successful extraction of photogenerated carriers is diminished. Because, transport and recombination are highly morphology dependent,[5] we hypothesize that any changes in transport/recombination due to photochemical degradation might also be morphology dependent. Such a morphology dependence could arise due to many factors ranging from composition-dependent photochemistry to morphology-dependent filamentary transport of charge carriers in the context of energetic disorder.[27, 15]

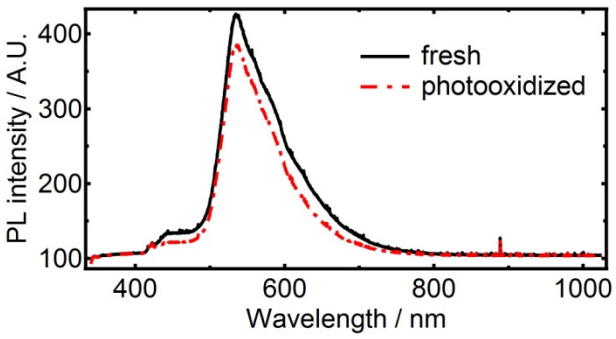

Figure 2.5 Photoluminescence spectrum of PFB:F8BT blend before (black solid line) and after (red dashed line) photooxidation with 6.0×10^{10} photons absorbed per μm^2.

To examine local variations in photooxidation with structure we employed trEFM. Fig. 6 shows an abbreviated schematic diagram of the trEFM apparatus that we use to measure the time rate of change of the capacitance and surface potential of a thin semiconductor film following illumination.[48, 9, 2] In this way, we can use trEFM as a non-contact method to measure spatial heterogeneity in local quantum efficiency due to both structural[9, 2] and photochemical factors.[48] More efficient regions of the device deliver photogenerated charges to the top surface of the film at a faster rate, leading to faster charging of the tip-sample capacitor.

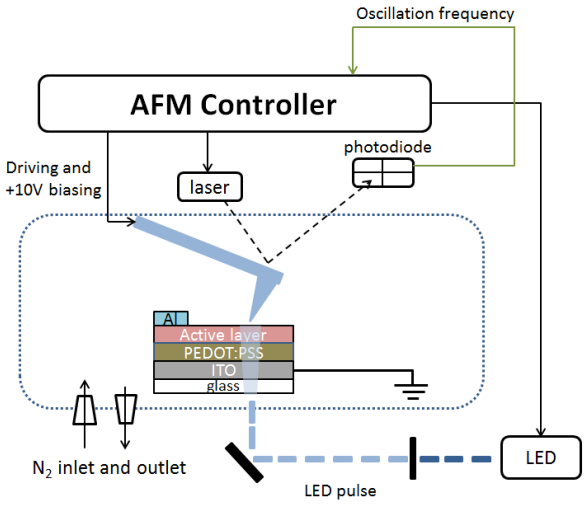

Figure 2.6 Schematic of trEFM setup. The sample was kept in a flow cell under a dynamic flow of dry N_2. The LED light was focused directly under the AFM tip to generate charges. The sample was grounded. +10V was applied to the tip. The oscillation frequency shift of the cantilever is due to changes in the capacitance gradient that result from the changes in the distribution of charge carriers underneath the tip. The exponential decay of oscillation frequency is fitted to extract the charging rates at each point.

As depicted in Fig. 6, we photodegraded films *in situ* using the same wavelengths (365 nm = preferential PFB excitation; 405 nm = equal PFB and F8BT excitation; and 455 nm = preferential F8BT excitation) that we used in the macroscopic photodiode experiments. In this way, we can directly image the relative changes in photocurrent arising from differences in photooxidation rates.

The top row of photooxidation in Fig. 7 shows trEFM images of the same area of a pristine PFB/F8BT blend collected with 365 nm, 405 nm, and 455 nm excitation sources. In each image the bright yellow regions correspond to faster photoinduced charging rates (more efficient local current generation and collection). The images show clear contrast, with the PFB-rich domains showing the fastest (most efficient) local rates when the film is excited at 365 nm or 405 nm. When the F8BT domains are preferentially excited the film shows more uniform contrast, but with distinct suppression of the photocurrent near the visible domain boundaries at 455 nm.

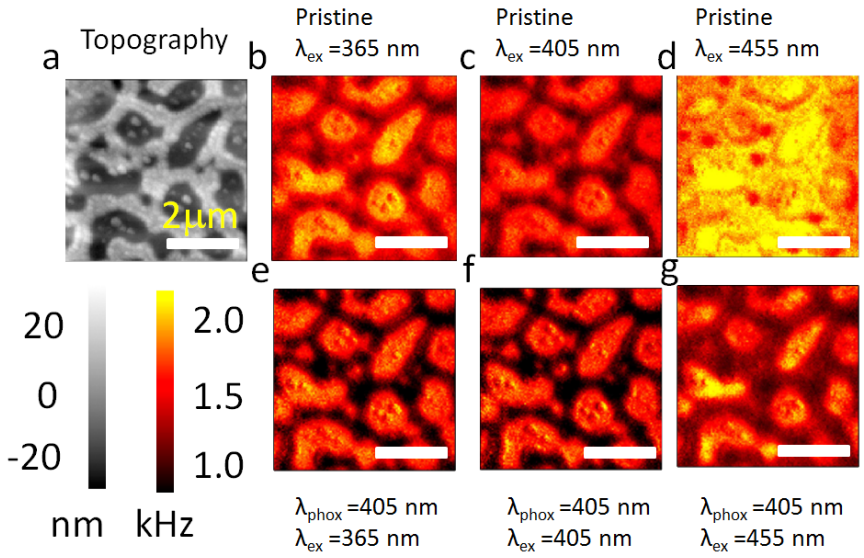

Figure 2.7 Charging rate maps of a given sample area. (a) The topography of the sample under investigation. (b-d) trEFM images scanned at 365 nm, 405 nm and 455 nm illumination, respectively, when the sample was pristine. (e-g) trEFM images scanned at 365nm, 405nm and 455nm illumination, respectively when the sample was photooxidized with 405 nm illumination.

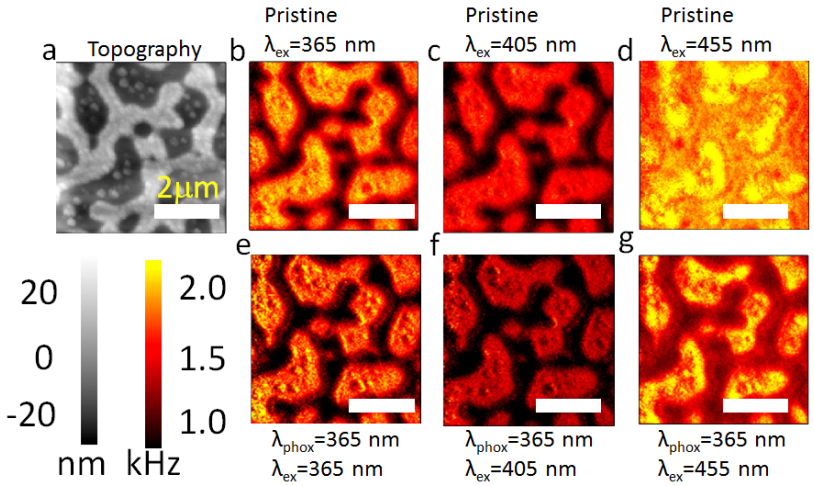

Figure 2.8 (a) The topography before photooxidation of a sample used in images b-g . (b-d) Charging rate maps with the same sample area as in (a), but generated by trEFM and scanned at 365 nm, 405 nm and 455 nm, respectively when the sample was fresh. (e-g) trEFM images scanned at 365nm, 405nm and 455nm, respectively after being photooxidized with 365 nm illumination.

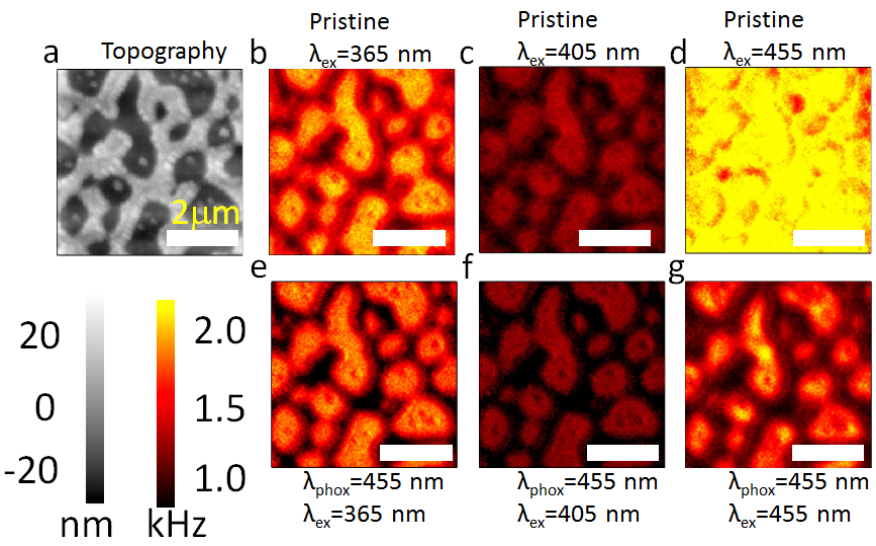

Figure 2.9 (a) The topography before photooxidation of a sample used in images b-g . (b-d) Charging rate maps with the same sample area as in (a), but generated by trEFM and scanned at 365 nm, 405 nm and 455 nm, respectively when the sample was fresh. (e-g) trEFM images scanned at 365nm, 405nm and 455nm, respectively after being photooxidized with 455 nm illumination.

The spatial contrast in the pristine PFB:F8BT films shown in Fig. 7b-d is a convolution of the compositionally-induced variations in light absorption at each location, and spatial variations in the quantum efficiency of the film. The local spatial variations in photocurrent collection in the PFB:F8BT system are known to be very sensitive to the exact film morphology, and undergo rapid changes in contrast near the 50: 50 blend composition used in this study.[32] Here, we have used only one blend composition, and our focus is instead on exploring how image contrast evolves after photooxidation.

To photooxidize the film, we exposed it to an absorbed dose of 6.0×10^{10} photons per μm^2 from a 405 nm LED while the samples were in ambient air. We then purged the sample cell with

dry nitrogen for 20 minutes, and re-imaged the samples with trEFM. Fig. 7e-g show the results, again probed with 365 nm, 405 nm, and 455 nm excitation. As expected, Fig. 7e-g all show slower photoinduced charging rates after photooxidation as would result from slower transport and increased recombination losses due to photochemically formed trap states.[48]

We note that Fig. 7b - 5g also show that the contrast between the different PFB-rich and F8BT-rich regions changes following photooxidation. Importantly, by comparing the charging rates before and after photooxidation in Fig. 7, we observe faster degradation rates in the regions of higher topography (F8BT-rich domains). For instance, under 455 nm illumination the charging rate goes from an overall almost homogeneous image (Fig. 7d) to one with strong contrast (Fig. 7g). Qualitatively similar results are obtained by photooxidizing at 365 nm or 455 nm (Fig. 8, 9). Even when the film is degraded with 365 nm light (preferential excitation of PFB), the strongest contrast in charging rate is observed by probing with 455 nm light (preferential excitation of F8BT), with the largest loss of charging rate occurring in the F8BT-rich regions. In other words, the trEFM data show that the F8BT-rich domains lose their ability to generate/harvest photocurrent faster than the PFB-rich domains. To better visualize the changes in trEFM charging contrast due to photooxidation, we plot the trEFM data as retained charging rate ratio images. We define the retained charging rate at each pixel as:

$$R_{CR} = \frac{k_{phox}}{k_{pristine}} \qquad \text{Equation 2.1}$$

where k_{phox} is the retained charging rate after photooxidation, and $k_{pristine}$ is the charging rate on the fresh film without photooxidation. Each sample area was imaged before and after

photooxidation at a single degrading wavelength, with the three probing wavelengths (365 nm, 405 nm and 455 nm).

Fig. 10 shows a 3x3 matrix of such retained charging rate (R_{CR}) images along with the associated film topography. The data shown correspond to 21 total scans, and 3 separate photooxidations. Bright areas are those that show little degradation after air/light exposure while dark areas are those that show significant degradation. These images provide dramatic visual evidence for our contention that the F8BT-rich regions of the film are losing their photocarrier generation/collection efficiency faster than the PFB-rich domains. Fig. 10d-10l show that regardless of what wavelength is used to photooxidize the film, and no matter what wavelength is used to photoexcite the film during for trEFM measurement the result is always the same: the F8BT-rich domains are darker in the ratio images, indicating they retained a smaller fraction of their initial efficiency after photooxidation. The images are all displayed with the same z-axis color scale. We do observe a greater extent of photooxidation in Fig. 10j, 10k and 10l, all probed with 455 nm, perhaps because this wavelength is preferentially absorbed by F8BT.

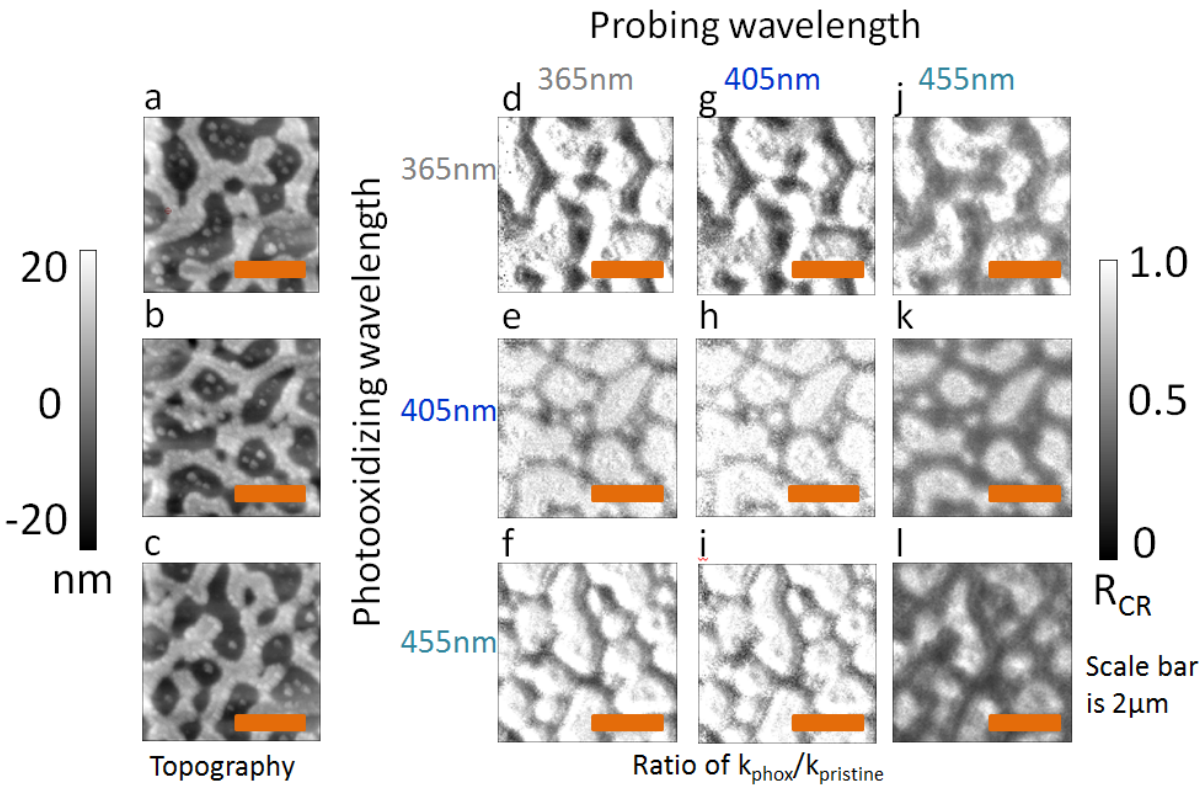

Figure 2.10 Charging ratio images of given areas. For each row, the image on the left hand side is the topography of area under investigation. (a) for (d, g, j), (b) for (e, h, k) and (c) for (f, i, l). For the 3×3 block on the right, each one is the charging ratio image before and after photooxidation. For example, each pixel in (e) is the charging rate ratio probed with 365 nm illumination before and after photooxidation with 405 nm illumination. All the charging rate ratio images share the same scale bar on the right. The average value of charging rate is lower when probing with 455 nm illumination.

Qualitatively, Fig. 10 shows clearly that, for all excitation wavelengths, the F8BT-rich domains are losing their ability to generate photocurrent more rapidly than the PFB-rich domains. A quantitative analysis (Table 1) shows that the degradation of the F8BT-rich domains is anywhere from 1.1-2.5X faster than the PFB-rich domains depending on the degradation and

probing wavelengths used. On the upper end, these ratios (Table 1) are just outside the ratio of F8BT concentration present in these domains, and one might thus interpret our data as indicating that degradation is simply linearly proportional to local F8BT concentration within a domain. However, an examination of the wavelength dependent data in Fig. 10 (and the ratios at different wavelengths, Table 1) shows that, at wavelengths where only F8BT absorbs, the response of the F8BT within the F8BT-rich regions is falling off *faster* than the response of the F8BT within the PFB-rich regions.

PFB-rich domains	Photooxodizing wavelength / nm		
Probing wavelength / nm	365	405	455
365	0.90	0.91	0.92
405	0.80	0.93	0.94
455	0.89	0.84	0.70

F8BT-rich domains	Photooxodizing wavelength / nm		
Probing wavelength / nm	365	405	455
365	0.71	0.77	0.52
405	0.66	0.87	0.54
455	0.52	0.53	0.30

Table 2.1 Quantitative analyses of the two domains under different photooxidizing and probing wavelengths.

The trEFM photooxidation data are not only consistent with the device data, but thus add a suggestive level of missing detail. Indeed, the trEFM data suggest that the reason that the F8BT photoresponse shown in Fig. 4 is falling off faster in the macroscopic photodiode measurements is because the regions where most of the F8BT absorption is taking place (the F8BT-rich domains) suffer from faster relative photooxidation overall.

These images provide important evidence in support of the hypothesis that local film structure will affect the local stability of the blend during photovoltaic operation. The origin of this local variation is a matter for speculation. It seems troubling that the F8BT-rich regions would lose performance fastest, as we would generally expect F8BT to be more oxidatively stable than PFB due to its greater ionization potential (Fig. 1).[47, 20] Indeed, when we subjected neat films of PFB and F8BT to photooxidation experiments characterized by grazing angle attenuated total reflection GATR-FTIR we found that at the same dosage PFB degrades much faster than F8BT, evidenced by the dramatic difference in keto-defect peak ~1720 cm^{-1}, Fig. 11. This is the carbonyl stretch of fluorenone.[48, 28] Keto-defects have been found to be electron trapping.[11] However, we point out that the photochemical reaction is a complex process which yields a variety of products. Their respective charge transport properties are not well investigated, and blends undergoing photoinduced charge transfer may react differently than pristine materials.

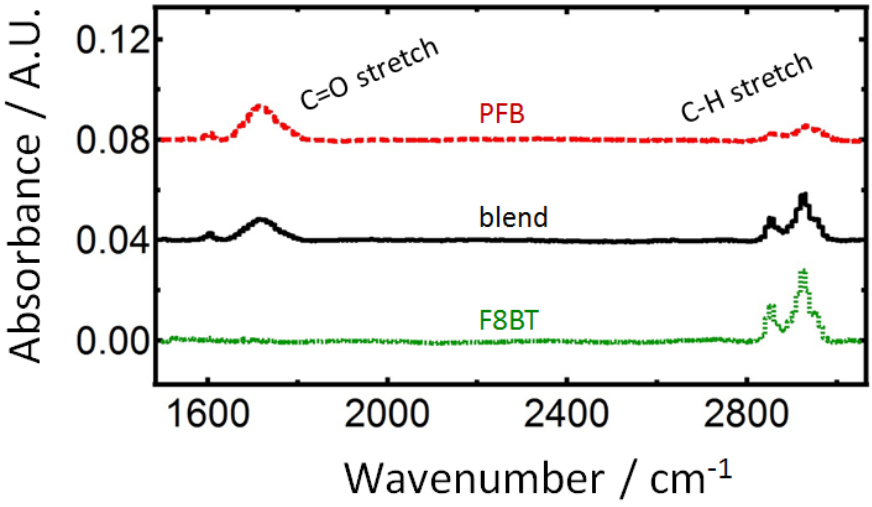

Figure 2.11 GATR-FTIR absorbance spectrum of PFB, blend and F8BT after photooxidation with absorbed photon dose of 2.0×10^{12}/μm2 with 405 nm LED. Ketone defect formation is indicated by C=O stretch ~1720 cm^{-1}.

In PFB/F8BT-based OLEDs it has been reported that dedoping of the PEDOT:PSS layers as a result of pinhole defects in the electrode could explain performance losses over time.[3] However, we do not believe such a mechanism can explain our *photo*-degradation data since the current density should be higher in the PFB-rich domains and lower in the F8BT-rich domains, thus, if the loss of device performance was from dedoping of the underlying PEDOT:PSS layer, we should expect the PFB-rich domains to degrade faster--which is the opposite of what we observe.

Given these contradictions, and the evidence for lower oxidative stability of our PFB relative to our F8BT samples, we speculate that the origin of the spatial variation in stability observed in Fig. 7, 8, 9 and 10 could be due to the breakdown of nanoscopic PFB hole transport pathways in the blend. Ironically then, our working hypothesis would suggest that the F8BT-rich domains are degrading fastest because they have a lower fraction of less stable PFB (typically ~10 %,[9] the exact composition may depend on the microscopic location, processing conditions such as spin-coating speed and temperature, but there is no doubt of dominance of F8BT in the F8BT-rich domains,[14, 9] making the few PFB-based hole-transport pathways that exist in those domains more susceptible to low levels of damage.

To test this hypothesis, we used conductive AFM (cAFM) to measure the hole current through the film injected by a gold tip. Due to the better alignment of the HOMO level of PFB with gold,[47, 20] hole current is predominantly carried by the PFB component in both phases in the blend, which is confirmed by Fig. 12b since there is a larger PFB composition in the lower

topography, PFB-rich regions.[9] After photooxidation with 405 nm at the photon dose used in trEFM, we observe a larger loss of hole current in the F8BT-rich phases shown in Fig. 12c. Fig. 12c is a hole current ratio image, defined as hole current post/pre photooxidation. Each pixel in the image is of the value:

$$R_{current} = \frac{I_{phox}}{I_{pristine}} \qquad \text{Equation 2.2}$$

where $I_{pristine}$ is the current before photooxidation, and I_{phox} is the current of the same pixel after photooxidation. The current ratio image suggests that proportionally, hole current loss is higher in the F8BT-rich domain than in the PFB-rich domain. If photooxidation were merely doping the polymer, we would expect a rise in the hole current.[19, 8] However, we see a drop of current over the entire image. This drop would be consistent with a breakdown of hole transport pathways due to photooxidation and we therefore conclude that our cAFM data are consistent with our hypothesis that the loss of photocurrent in the F8BT-rich domains could be from the degradation of hole transport pathways. However, we point out that this hypothesis will still need to be tested further, and hope our findings will stimulate future experimentation.

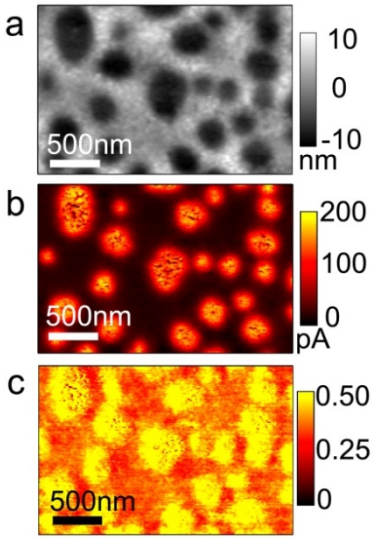

Figure 2.12 Current image of a PFB:F8BT blend after photooxidation. (a) is the topography image of the sample area. (b) is the current image of pristine sample under 5V bias. (c) is the retained current ratio image plotting the ratio of injected hold current before and after photooxidation, showing that while the PFB-rich domains have much higher hole injection current densities in both cases, the F8BT-rich domains show the biggest proportional decrease in hole current following photooxidation.

2.4 Conclusions

We have used a combined study of trEFM and device EQE measurements to show that the rate of device aging in nanostructured polymer solar cells can depend on local composition in a model polyfluorene copolymer blend solar cell. After photooxidizing the films we observed that the device EQE spectra show a reduced contribution from the spectral region attributable to F8BT absorption. Importantly, the *in situ* trEFM data show that this result can be explained by a relatively faster decay of the photocurrent contributions from the F8BT-rich domains to the net device photocurrent, even while the F8BT present in PFB-rich domains appears to continue to

contribute to the device photocurrent. Consistent with our FTIR and cAFM data, we speculate that this differential degradation could be the result of broken percolation networks of the minority PFB chains within the F8BT-rich networks. Overall, these data show that local compositional heterogeneity can affect device aging, and that an understanding of photochemical degradation and trap formation on the nanoscale could prove invaluable in understanding and improving the lifetime performance of organic solar cells.

2.5 References

1. J. J. M. Halls, C. A. Walsh, N. C. Greenham, E. A. Marseglia, R. H. Friend, S. C. Moratti and A. B. Holmes, *Nature*, 1995, **376**, 498-500.
2. G. Yu, J. Gao, J. C. Hummelen, F. Wudl and A. J. Heeger, *Science*, 1995, **270**.
3. http://www.polyera.com/, 2012.
4. http://www.heliatek.com/, 2012.
5. http://newsroom.ucla.edu/portal/ucla.
6. K. M. Coakley and M. D. McGehee, *Chemistry of Materials*, 2004, **16**, 4533-4542.
7. B. Kippelen and J.-L. Bredas, *Energy & Environmental Science*, 2009, **2**, 251-261.
8. F. C. Krebs, S. A. Gevorgyan and J. Alstrup, *Journal of Materials Chemistry*, 2009, **19**, 5442-5451.
9. C. Groves, O. G. Reid and D. S. Ginger, *Accounts of Chemical Research*, 2010, **43**, 612-620.
10. M. Jorgensen, K. Norrman and F. C. Krebs, *Solar Energy Materials and Solar Cells*, 2008, **92**, 686-714.

11. M. O. Reese, A. M. Nardes, B. L. Rupert, R. E. Larsen, D. C. Olson, M. T. Lloyd, S. E. Shaheen, D. S. Ginley, G. Rumbles and N. Kopidakis, *Advanced Functional Materials*, 2010, **20**, 3476-3483.

12. M. O. Reese, A. J. Morfa, M. S. White, N. Kopidakis, S. E. Shaheen, G. Rumbles and D. S. Ginley, *Solar Energy Materials and Solar Cells*, 2008, **92**.

13. X. N. Yang, J. K. J. van Duren, R. A. J. Janssen, M. A. J. Michels and J. Loos, *Macromolecules*, 2004, **37**.

14. A. Seemann, T. Sauermann, C. Lungenschmied, O. Armbruster, S. Bauer, H. J. Egelhaaf and J. Hauch, *Solar Energy*, 2011, **85**, 1238-1249.

15. L.-M. Chen, Z. Hong, G. Li and Y. Yang, *Advanced Materials*, 2009, **21**, 1434-1449.

16. S. K. Hau, H.-L. Yip, N. S. Baek, J. Zou, K. O'Malley and A. K. Y. Jen, *Applied Physics Letters*, 2008, **92**.

17. M. Drees, H. Hoppe, C. Winder, H. Neugebauer, N. S. Sariciftci, W. Schwinger, F. Schaffler, C. Topf, M. C. Scharber, Z. Zhu and R. Gaudiana, *Journal of Materials Chemistry*, 2005, **15**, 5158-5163.

18. F. C. Krebs and H. Spanggaard, *Chemistry of Materials*, 2005, **17**, 5235-5237.

19. B. J. Kim, Y. Miyamoto, B. Ma and J. M. J. Frechet, *Advanced Functional Materials*, 2009, **19**, 2273-2281.

20. F. C. Krebs and K. Norrman, *Progress in Photovoltaics: Research and Applications*, 2007, **15**, 697-712.

21. H. Bassler, G. Schonherr, M. Abkowitz and D. M. Pai, *Physical Review B*, 1982, **26**, 3105-3113.

22. W. F. Pasveer, J. Cottaar, C. Tanase, R. Coehoorn, P. A. Bobbert, P. W. M. Blom, D. M. de Leeuw and M. A. J. Michels, *Physical Review Letters*, 2005, **94**.

23. J.-M. Zhuo, L.-H. Zhao, R.-Q. Png, L.-Y. Wong, P.-J. Chia, J.-C. Tang, S. Sivaramakrishnan, M. Zhou, E. C. W. Ou, S.-J. Chua, W.-S. Sim, L.-L. Chua and P. K. H. Ho, *Advanced Materials*, 2009, **21**, 4747-4752.

24. M. S. A. Abdou, F. P. Orfino, Y. Son and S. Holdcroft, *Journal of the American Chemical Society*, 1997, **119**, 4518-4524.

25. D. C. Coffey, O. G. Reid, D. B. Rodovsky, G. P. Bartholomew and D. S. Ginger, *Nano Letters*, 2007, **7**, 738-744.

26. L. S. C. Pingree, O. G. Reid and D. S. Ginger, *Advanced Materials*, 2009, **21**, 19-28.

27. R. Giridharagopal and D. S. Ginger, *The Journal of Physical Chemistry Letters*, 2010, **1**, 1160-1169.

28. O. G. Reid, G. E. Rayermann, D. C. Coffey and D. S. Ginger, *The Journal of Physical Chemistry C*, 2010, **114**, 20672-20677.

29. N. Balke, D. Bonnell, D. S. Ginger and M. Kemerink, *Mrs Bulletin*, 2012, **37**, 633-637.

30. J. R. O'Dea, L. M. Brown, N. Hoepker, J. A. Marohn and S. Sadewasser, *Mrs Bulletin*, 2012, **37**.

31. E. Sengupta, A. L. Domanski, S. A. L. Weber, M. B. Untch, H.-J. r. Butt, T. Sauermann, H. J. Egelhaaf and R. d. Berger, *The Journal of Physical Chemistry C*, 2011, **115**, 19994-20001.

32. D. C. Coffey and D. S. Ginger, *Nat Mater*, 2006, **5**, 735-740.

33. R. Giridharagopal, G. E. Rayermann, G. Shao, D. T. Moore, O. G. Reid, A. F. Tillack, D. J. Masiello and D. S. Ginger, *Nano Letters*, 2012, **12**, 893-898.

34. A. C. Arias, J. D. MacKenzie, R. Stevenson, J. J. M. Halls, M. Inbasekaran, E. P. Woo, D. Richards and R. H. Friend, *Macromolecules*, 2001, **34**, 6005-6013.

35. H. J. Snaith, A. C. Arias, A. C. Morteani, C. Silva and R. H. Friend, *Nano Letters*, 2002, **2**, 1353-1357.

36. R. Stevenson, A. C. Arias, C. Ramsdale, J. D. MacKenzie and D. Richards, *Applied Physics Letters*, 2001, **79**, 2178-2180.

37. T. J. K. Brenner and C. R. McNeill, *The Journal of Physical Chemistry C*, 2011, **115**, 19364-19370.

38. C. R. McNeill, B. Watts, L. Thomsen, H. Ade, N. C. Greenham and P. C. Dastoor, *Macromolecules*, 2007, **40**, 3263-3270.

39. E. Moons, *Journal of Physics-Condensed Matter*, 2002, **14**, 12235-12260.

40. A. C. Morteani, A. S. Dhoot, J. S. Kim, C. Silva, N. C. Greenham, C. Murphy, E. Moons, S. Cina, J. H. Burroughes and R. H. Friend, *Advanced Materials*, 2003, **15**.

41. N. Tessler, Y. Preezant, N. Rappaport and Y. Roichman, *Advanced Materials*, 2009, **21**, 2741-2761.

42. R. Coehoorn, W. F. Pasveer, P. A. Bobbert and M. A. J. Michels, *Physical Review B*, 2005, **72**.

43. L. L. Liu, S. Tang, M. R. Liu, Z. Q. Xie, W. Zhang, P. Lu, M. Hanif and Y. G. Ma, *Journal of Physical Chemistry B*, 2006, **110**, 13734-13740.

44. X. H. Yang, F. Jaiser, D. Neher, P. V. Lawson, J. L. Bredas, E. Zojer, R. Guntner, P. S. de Freitas, M. Forster and U. Scherf, *Advanced Functional Materials*, 2004, **14**, 1097-1104.

45. J. S. Kim, P. K. H. Ho, C. E. Murphy, N. Baynes and R. H. Friend, *Advanced Materials*, 2002, **14**, 206-209.

46. E. J. Meijer, C. Detcheverry, P. J. Baesjou, E. van Veenendaal, D. M. de Leeuw and T. M. Klapwijk, *Journal of Applied Physics*, 2003, **93**, 4831-4835.

Chapter 3

Probing Charge Carrier Lifetime at the Buried Interface in Organic Photovoltaics with Frequency-Modulated Scanning Kelvin Probe Microscopy

3.1 Introduction

The power conversion efficiency (PCE) of organic photovoltaics has reached ~10% in single layer device,[1] with an increase from ~2% in the past decade. Bearing the potential benefit of roll-to-roll processing and large-scale production, it is a promising form of alternative energy. Despite the ultrafast charge generation, extracted charges in OPV remain much lower than predicted. Recombination is limiting the charge carrier density and what could be extracted from the photogenerated charges. Organics/electrode interface controls the energy level alignments and local electrostatic field.[2,3] It affects the band bending and charge recombination near the electrode. Different surface modifiers have been used on different samples to tune the open-circuit voltage, which also affects the band bending and recombination in the organic layer.

Recombination of electrons and holes in the polymer is a bimolecular process, described by Langevin recombination $R = k \cdot n \cdot p$, where k is the reaction constant, n and p are the electron and hole concentration, respectively. k is determined by

$$k = \frac{\mu_n + \mu_p}{\varepsilon} \cdot e \cdot N_A \cdot coef \qquad \text{Equation 3.1}$$

where μ_n and μ_p are the mobilities for electron and hole, respectively, ε is the dielectric constant, e is the elementary charge, N_A is Avogadro's number, coef is a unitless scaling coefficient. Both electron and hole mobilities are carrier density dependent, due to the disorder present within the polymer/fullerene blend.

Charge carrier mobilities in organic solar cells are carrier density dependent. Thus the bimolecular reaction constant increases with charge carrier density. Thus the charge carrier lifetime at a given carrier concentration could not be predicted. Measurement of charge carrier mobility on the microscopic scale is needed to interpret the role of microstructure on recombination kinetics.

Studying of recombination and microstructures of OPV have largely been two separate processes. Recombination could be carried out in photoinduced spectroscopy,[4] while structure of the film is examined by X-ray scattering/absorption based technique,[5,6] or energy filtered transmission electron microscopy.[7] *A priori* knowledge on origins and destinations of different photogenerated species are required to interpret the results.[4,8] Thus simultaneous information on the thin film microstructure and recombination rate would be desirable.

Atomic Force Microscopy has been successful at characterizing morphology dependent charge generation at the microscopic scale.[9,10] Scanning Kelvin Probe Microscopy was demonstrated to characterize the increased recombination after device degradation. Frequency-modulated Scanning Kelvin Probe Microscopy (FM-SKPM) has also been used to determine the charge carrier recombination rate in silicon solar cells,[11] which is relatively insensitive to charge carrier density. Here we extend this technique to study the carrier density-dependent recombination rate in organic cells on microscopic scale. In this chapter, we will show that in analogy to Trasient Photovoltage (TPV) measurement, with both perturbation and background illumination in place, we examine the transient process in SKPM by frequency modulating the probing light, combined with numerical simulations. We obtained insights on the charge carrier lifetime in organic photovoltaics sample under the SKPM setup.

3.2 Materials and Methods

Bulk heterojunction solar cell made from 1:4 weight ratio PCDTBT (poly[*N*-11″-henicosanyl-2,7-carbazole-alt-5,5-(4′,7′-di-2-thienyl-2′,1′,3′-benzothiadiazole)]):$PC_{71}BM$ (phenyl-C_{71}-butyric acid methyl ester) was dissolved in a mixed solvent of 2:1 volume ratio of 1, 2, 4-tricholorobenzene (TCB):dicholorobenzene (DCB). The solution was spin coated on top of a 30 nm PEDOT:PSS layer in N_2 glovebox to form a 70 nm active layer. For J-V curve and device measurement, a top contact of 40 nm Al top contact was evaporated. No top contact was evaporated for the sample prepared for SKPM experiments.

AFM. SKPM measurements were carried out on MFP-3D-BIO (Asylum Research) based AFM with custom modifications using 300 kHz Pt-coated cantilevers (BudgetSensor ElectriTap300). SKPM was carried out in a flow cell, at a lift height of 50 nm. The flow cell used here has a 1.50-2.55 mL fluid volume after engaging the tip. FM-SKPM setup is displayed in Fig. 1b. Being different from the setup used by Takahashi,[11] two light sources were used. The white LED acted as the background illumination with varying intensities from 0, 1% to 3% of 1.5 AM one sun intensity. Blue LED was modulated with different frequency as the probing light. The surface potential over a single point was recorded over time. As shown in Fig. 1c, V_a is the absolute value of photovoltage caused by the white illumination. On top of that, V_b is the total change of photovoltage resulting from both the blue perturbation and the white background. Due to the quick saturation of surface photovoltage with intensity, as shown in Fig. 2, a large perturbation was used to introduce large enough signal to be probed. The probing intensity was 12.5% while the background changes from 0%, 1% to 3%. The 455 nm LEDs were purchased from LED Engin (product numbers LZ1-00DB00). Incident illumination power was calibrated using a Si diode.

Transient Photovoltage and Charge Extraction Measurements. TPV and CE measurements were performed on a home-built system.[2] Background illumination was provided by a white LED (Bridgelux BXRA-56C9000-J) which was driven by a TTI instrument power supply (CPX400SA) and controlled through custom LabVIEW program. A 447.5 nm LED (Luxeon Star LXML-PR01-0425) was pulsed (2 Hz, 4 μs width, 20 ns edge) by a home-built LED driver circuit and waveform generator (Agilent

33210A) were used to generate a voltage transient measured by an oscilloscope (Textronix TDS 2024B). Samples were mounted in a home-built vacuum chamber and tested under active vacuum (typically between 5 and 15 mTorr).

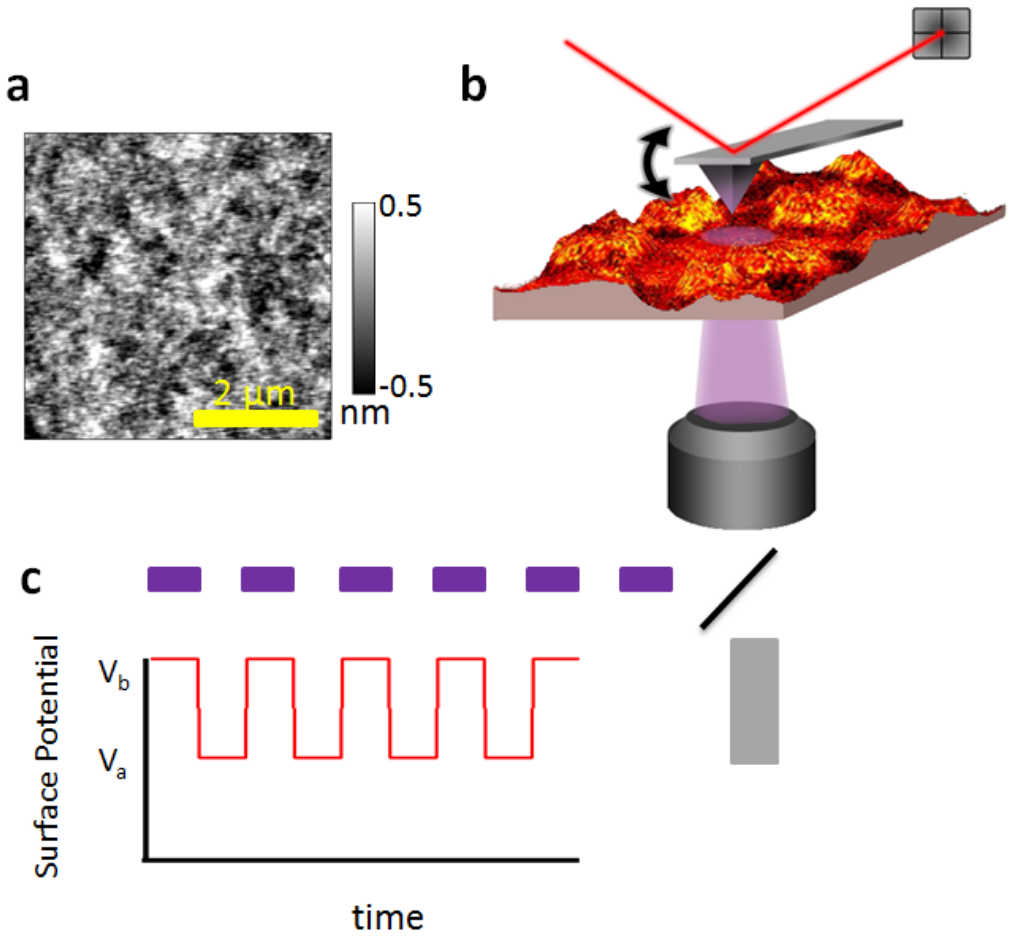

Figure 3.1 SKPM of experiment on the sample of PCDTBT:$PC_{71}BM$. a) shows the topography of a typical sample area. b) shows the setup of the frequence modulated SKPM, with the white background illumination and blue modulation illumination coming both under the AFM tip. c) shows the surface potential probed by the AFM tip, V_b is the surface potential when both white and blue illuminations are incident, V_a is of that when only white illumination is present.

3.3 Results and Discussion

As shown in Fig. 1a, the film topography measured with AFM is smooth on the 100 nm scale, with an RMS roughness < 1 nm. Device of PCE 4.2% was achieved under one sun 1.5 AM, with a V_{oc} of 0.89 V and Jsc of 11.2 mA/cm^2. The V_{oc} and Surface photovoltage (SPV) values at different light intensities are displayed in Fig. 2. V_{oc} is the voltage at which the current is zero on a device J-V curve, SPV is the change of surface potential value upon illumination. V_{oc} and SPV demonstrate similar behavior under illumination, quickly saturating near 1.5 AM one sun intensity.

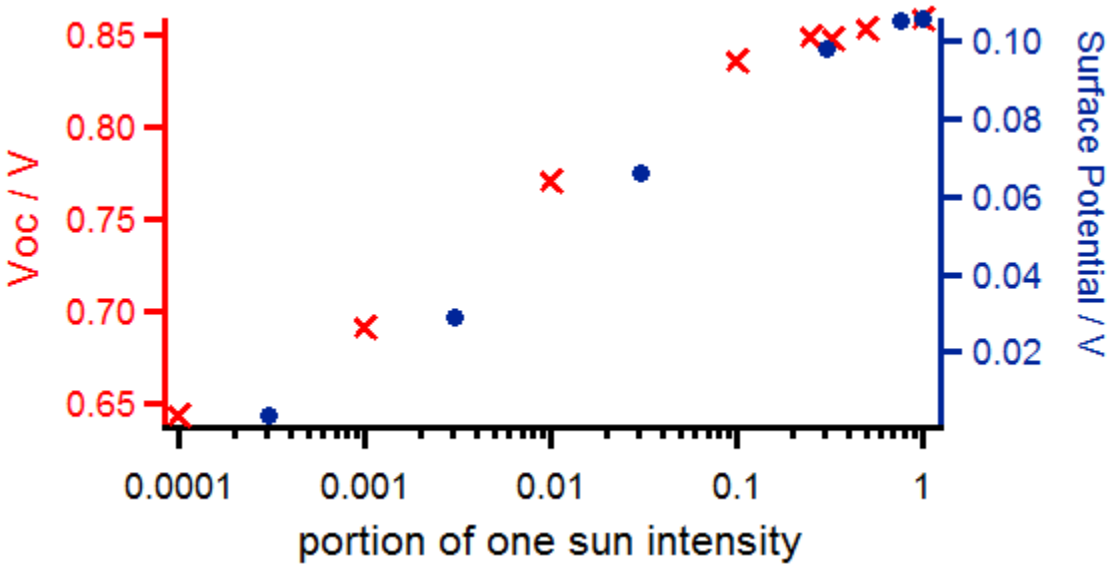

Figure 3.2 Voc measured from device (red crosses) and surface potential measured from SKPM (blue dots) at different light intensities.

Next we carried out the FM-SKPM experiment with two beams to emphasize the carrier density dependent recombination rate. As the background white light intensity increases, so does charge carrier intensity. However, the increase of V_{oc} slows down with increase in light intensity due to the faster and faster charge recombination rate. Red trace in Fig. 2 shows V_{oc} *vs.* light intensity. V_{oc} of PCDTBT:$PC_{71}BM$ almost instantly rises to ~0.65 V at very low light intensities, ~0.01% sun, and saturate ~ 1 sun to ~0.89 V. The change of surface photovoltage (SPV) probed by SKPM is shown in the blue trace, being similar to the trend of V_{oc}, it also saturates ~ 1sun. However, the change of SPV is a much smaller value over the whole range of intensity. The reason is that V_{oc} measures the splitting between the donor/acceptor HOMO/LUMO. SPV, defined as the change of surface potential caused by incident illumination, is the averaged shift in Fermi level of areas in proximity to AFM probe due to accumulation of charge carriers, which is also results of change in built-in field, V_{bi}. The small and quick saturation *vs.* illumination intensity implies that modulating blue illumination intensity has to be larger or at least comparable to the background illumination to induce enough amount of change in surface photovoltage, otherwise photovoltage induced by the perturbation would be buried in background. This means the perturbation would not remain small relative to the white background illumination. Instead it will produce a significant number of charge carriers upon the background during whose decay would experience through the different levels of charge carrier density, thus different recombination rates. As a result, the apparent decay of photovoltage in SKPM would manifest itself as sum of multiple exponential functions.

The time averaged surface potential values are displayed in Fig. 3. The red, blue and green crosses are experimental data of time averaged SPV at different modulating frequency of the 12.5% sun intensity of blue LED. The background intensities are 0, 1% and 3% for the red, blue and green dots respectively. The lines are frequency domain stretched exponential fit (Equation 3.2) to the experimental data. Different from the Si solar cell lifetime, here in the PCDTBT:$PC_{71}BM$ blend, the decay of charge carriers become faster at higher background intensities, which suggests the charge carrier lifetime is density dependent. This was not observed when Takahashi did the experiment on Si.[11]

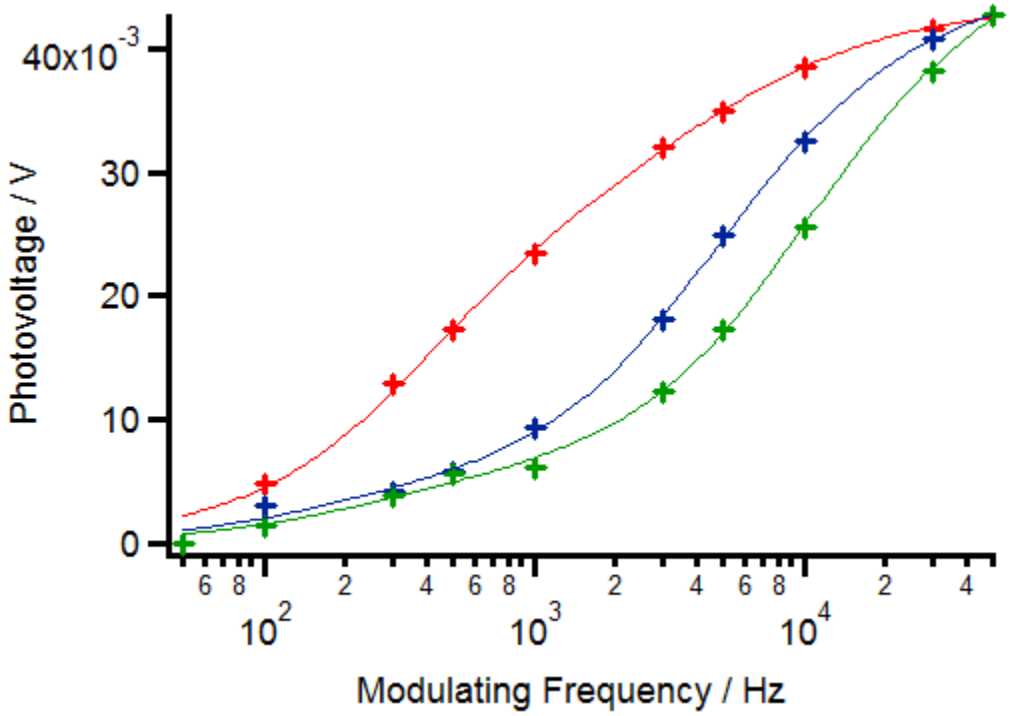

Figure 3.3 Average of surface photovoltage measured at different modulating frequencies in SKPM. The photovoltage shown on the left axis is the absolute value of the difference between light on and off. In all cases there is blue illumination of 13% of one sun intensity. For the red trace, there is no background illumination; for the blue

trace, there is background illumination with intensity of 1% of one sun intensity; for the green trace, there is background illumination with intensity of 3% of one sun intensity.

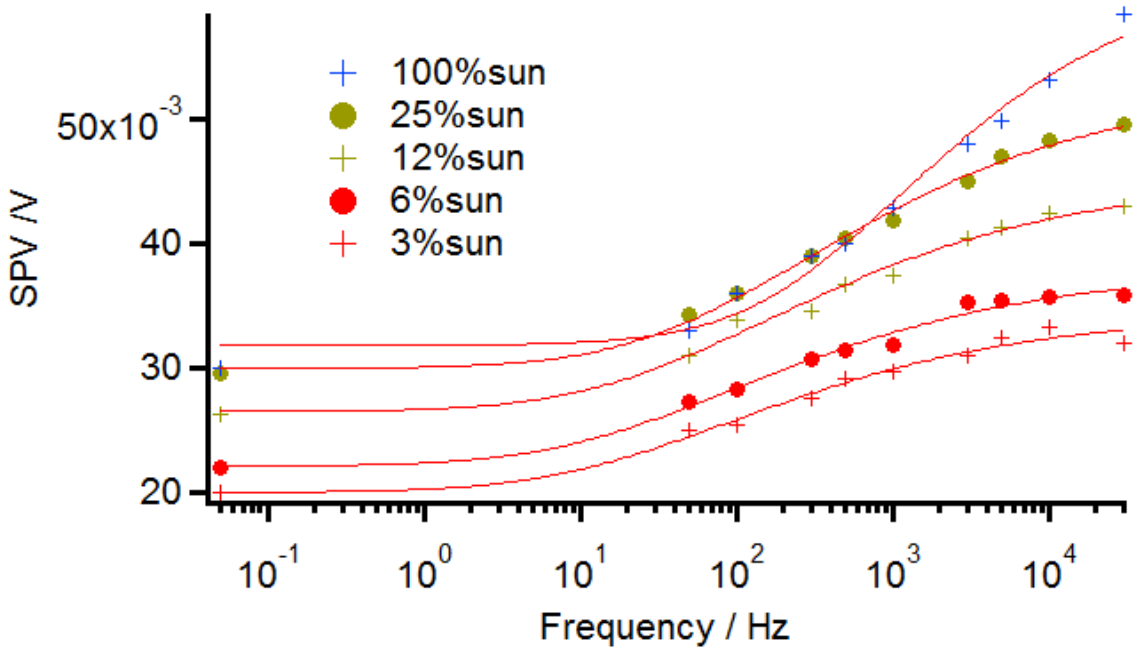

Figure 3.4 FM-SKPM results under different probing illumination intensity. Each point in the figure corresponds to time averaged SPV over the whole time of modulation. Intensities are color-coded, shown in the figure. Solid lines are frequency domain stretched exponential decay fit to the data.

To be quantitative on the lifetime of charge carriers, a series of experiments were carried out with varying probing light intensities (without background illumination). Results are shown in symbols in Figure 3.4, as the probing light intensity goes up, both the signal magnitude and decay rate increase. The lines in Figure 3.4 were also fits with frequency domain stretched exponential decay as in Equation 3.2, assuming the decay of

SPV is composed of a distribution of decay pathway of different rates. The time-averaged photovoltage within a cycle of the perturbation is integrated as a function of modulating frequency, expressed in Equation 3.2.

$$V_{avg} = \frac{V_0}{2} + \frac{V_0 \tau f \Gamma\left(\frac{1}{b}, \left(\frac{1/2f}{\tau}\right)^b\right)}{b} \qquad \text{Equation 3.2}$$

where V_0 is the SPV caused by illumination, τ is the characteristic lifetime of the stretched exponential decay, b is the stretching exponent, f is the modulating frequency. The fitted characteristic lifetime is shown in Figure 3.8. Characteristic lifetime of FM-SKPM keeps decreasing as probing light intensity goes up to one sun. Again this confirms the carrier density dependent recombination rate.

The experiments carried out under FM-SKPM with (Figure 3.3) and without (Figure 3.4) background illumination both suggest concentration dependent charge recombination rate. To obtain the information on density dependent lifetime, the same device was tested under TPV setup, where the sample is illuminated with a constant white background and a weak pulsed blue light. Tuning of the white background intensity allows controlling of background carrier density, while the blue pulsed light creates a <20 meV bias above the background V_{oc}. This small perturbation of charge carriers has little effect on the overall charge carrier density. At the same time, the decay of ΔV_{oc} encodes the lifetime of charge carriers at this background density. Exponential fit to ΔV_{oc} *vs.* time yields the lifetime of carriers. As shown in Figure 3.4, the carrier lifetime decreases exponentially with increasing carrier concentration.

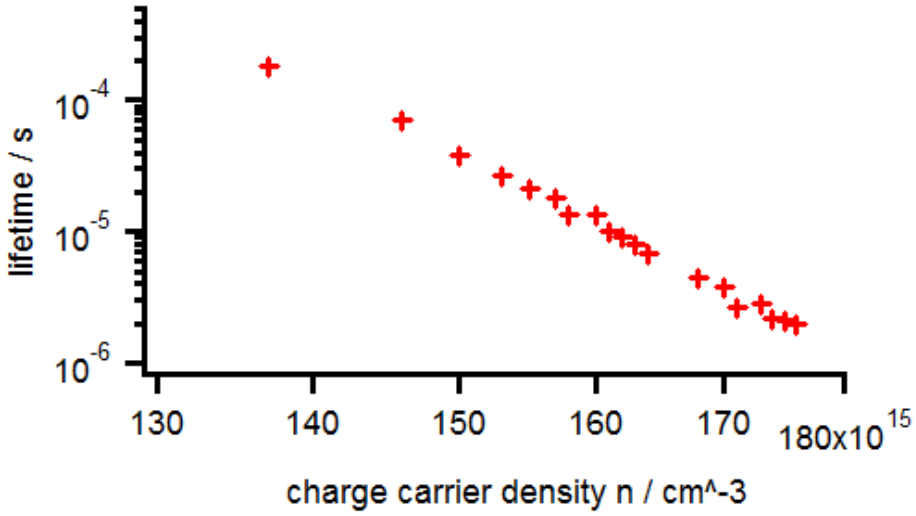

Figure 3.5 Lifetime of charge carriers measured at different carrier densities by varying the illumination intensity, measured through TPV.

This concentration dependent carrier lifetime as shown in Figure 3.5 is the reason for intensity dependent SPV lifetime. Since a large probing intensity of 12.5% sun was used in the FM-SKPM experiment, after the probing light turned off, the carrier density would change over a wide range of values, each with its respective lifetime. In Figure 3.3, when the background intensity was raised, both the higher and lower limit on the sampling concentration range increased, thus averaged carrier lifetime decreased overall. On the other hand, in Figure 3.4, without background illumination, when the probing intensity increased, the starting point would be raised, decreasing the averaged carrier lifetime as well.

Due to the low time resolution, with the purpose of monitoring the surface photovoltage (SPV) decay rate, FM-SKPM is actually measuring the time-averaged SPV. Thus to compare with TPV measured lifetime, we have to convert the V_{oc} *vs.* time

behavior into a time averaged value. At first glance, it seems quite straight forward to use directly record V_{oc} decay vs. time as shown in Figure 3.6 and translate that into the frequency domain. The pitfall here is that at longer times, ~ 1 ms, the lifetime measured by TPV is restricted by RC time constant of the circuit.[2,12]

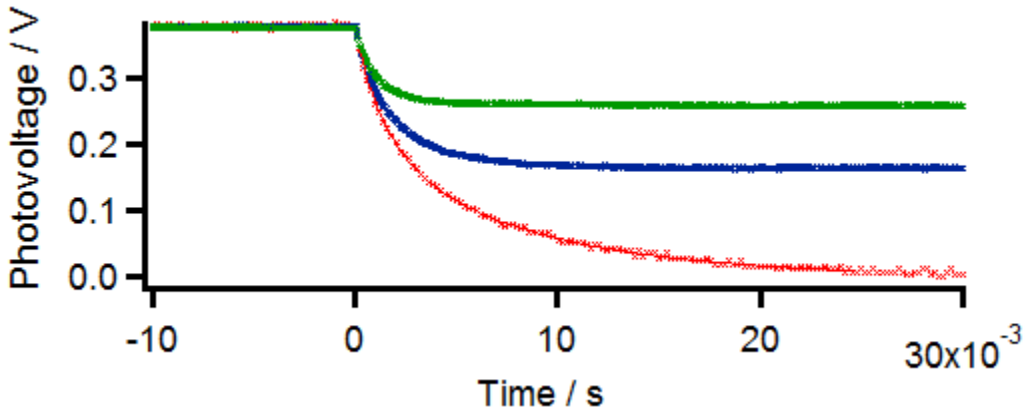

Figure 3.6 Decay of photovoltage measured across a device with different illuminations. In all cases the decay starts with the event of turning off the blue illumination which is 12.5% of one sun intensity. For the red trace, there is no background illumination; for the blue trace, there is background illumination with intensity of 1% of one sun intensity; for the green trace, there is background illumination with intensity of 3% of one sun intensity. The green and blue traces are shifted to align with red trace to easier comparison. The lifetime obtained from these raw decay curves are convoluted with RC time constant.

It turns out that to disentangle RC time constant from the real recombination process we need to simulate the TPV response based on the raw data of lifetime, carrier

concentration and V_{oc}. Empirical relations between these parameters have been explored previously to shed light on the recombination kinetics of charge carriers inside organic photovoltaics.[13] Red lines in Figure 3.7a, b, c are fits to the following equations, respectively.

$$tau = tau_0 \cdot \exp(-\beta V_{oc}) \quad \text{Equation 3.3}$$

$$n = n_0 \cdot \exp(\gamma V_{oc}) \quad \text{Equation 3.4}$$

$$tau = tau_0 \cdot (\frac{n_0}{n})^{\lambda} \quad \text{Equation 3.5}$$

Where tau is the carrier lifetime, V_{oc} is the open circuit voltage and n is carrier concentration, tau_0, n_0, β, γ, λ are fitting constants. In the end, carrier concentration decay rate is described by the following equation

$$\frac{dn}{dt} = -\frac{n^{1+\lambda}}{(1+\lambda)\cdot tau_0 \cdot n_0^{\lambda}} \quad \text{Equation 3.6}$$

Combined with the initial carrier concentration, Equation 3.4 would allow us to simulate the decay of carrier concentration *vs.* time, which leads us to know the V_{oc} vs. time curve according to Equation 3.2. Assuming no charge recombination happens in the charge extraction process, simulation of Voc decay *vs.* time based on Equation 3.4 is the ideal way to yield information on the recombination limited, rather than RC time limited, decay of V_{oc}.

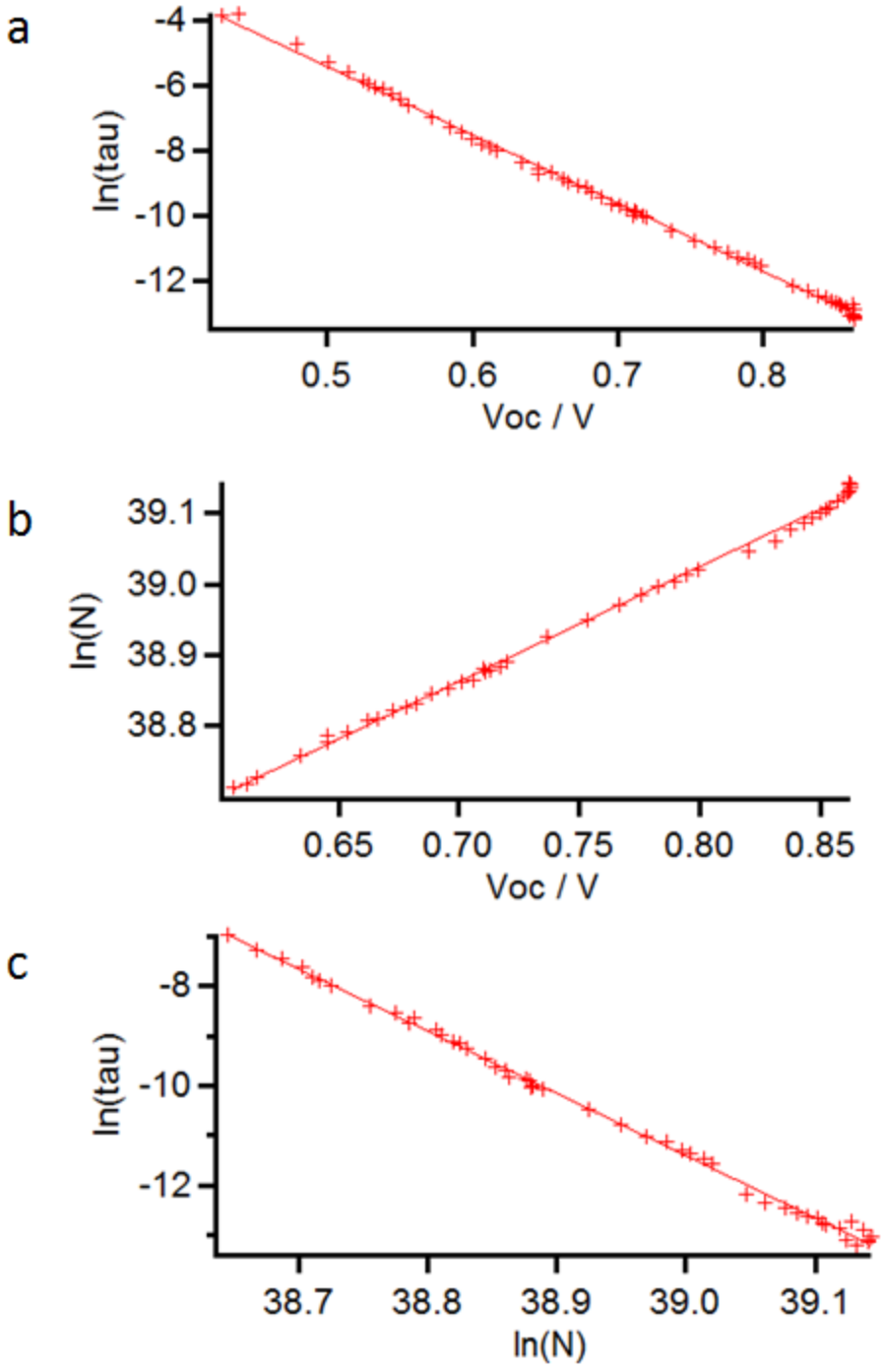

Figure 3.7 Relations of charge carrier lifetime (tau) *vs.* open circuit voltage (V_{oc}) (a), carrier density (N) *vs.* V_{oc} (b) tau *vs.* N (c), as discussed in ref[13]. These curve combined would allow us to simulate carrier density decay *vs.* time without convoluted by RC time constant.

As shown in Figure 3.8a, within one period which corresponds to a modulating frequency in FM-SKPM, during the first half period V_{oc} stay at light on position, as the light turns off at the start of the second half period, V_{oc} starts to decay till the end of the modulating period. V_{oc_avg} is the time average of V_{oc} for the whole modulating period. Each point in Figure 3.8b is a time averaged data.

TPV data in Figure 3.8b are fitted with frequency domain stretched exponential decay (Equation 3.2). Results here are in Figure 3.9 to compare with the FM-SKPM lifetime. As we can see, the lifetime of TPV remain largely constant throughout the whole intensities range. This is caused by the relative slow decay of V_{oc} at long time. At the same time, FM-SKPM lifetime decreases over an order of magnitude, leading us to believe there is a quick decay in SPV which only appeared as probing light intensity is high enough, as evidence in Figure 3.10. In Figure 3.10, SPV of the device is shown in red, represented on the left axis. On the right axis is the portion of SPV at 30 kHz in full SPV, which means the ratio of the averaged SPV measured at 30 kHz divided by the SPV when the light is full on. The steep slope of the blue curve as light intensity goes from 100% to 25% indicates there is a quick decay in SPV. This observation reminds us to measure lifetime of FM-SKPM decay under even higher light intensities to capture the dynamics of this fast process. Correspondingly, we need to raise the background illumination to the same level in order to make a comparison. The alternative way is to introduce background illumination into FM-SKPM experiment which will enable the system to endure only the fast decay process. The intensity ratio of background and probing illumination is yet to be optimized to maximize S/N.

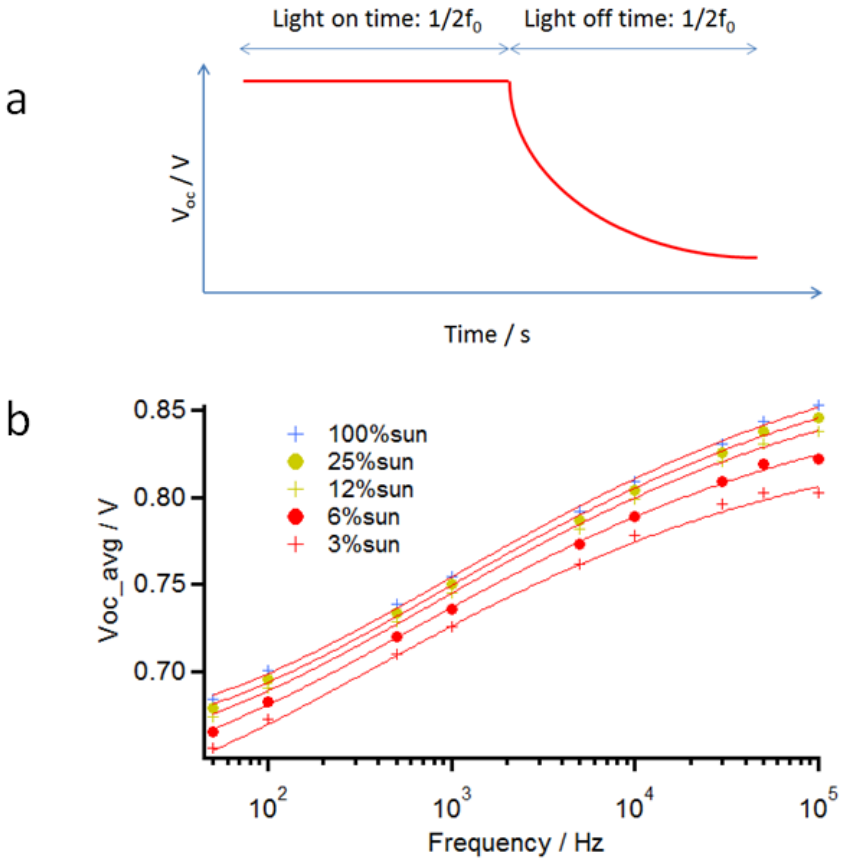

Figure 3.8 (a) describes how the time average of V_{oc} is taken. In a complete modulation period, during the first half of light staying on, it is a flat line. As light turns off at the beginning of the second half, V_{oc} starts to decay, till the light turns on again. V_{oc} is integrated over the whole modulation period and divided by the period to extract time averaged V_{oc}. (b) is the time averaged Voc using different modulation frequencies and light intensities. Solid lines are frequency domain stretched exponential decay fit to the dots.

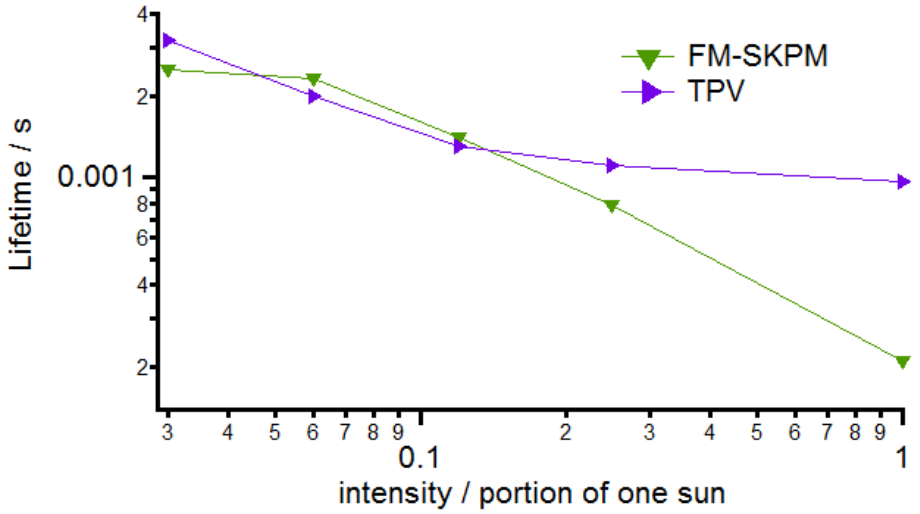

Figure 3.9 Characteristic lifetimes of SPV decay and TPV decay based on frequency domain stretched exponential decay fit.

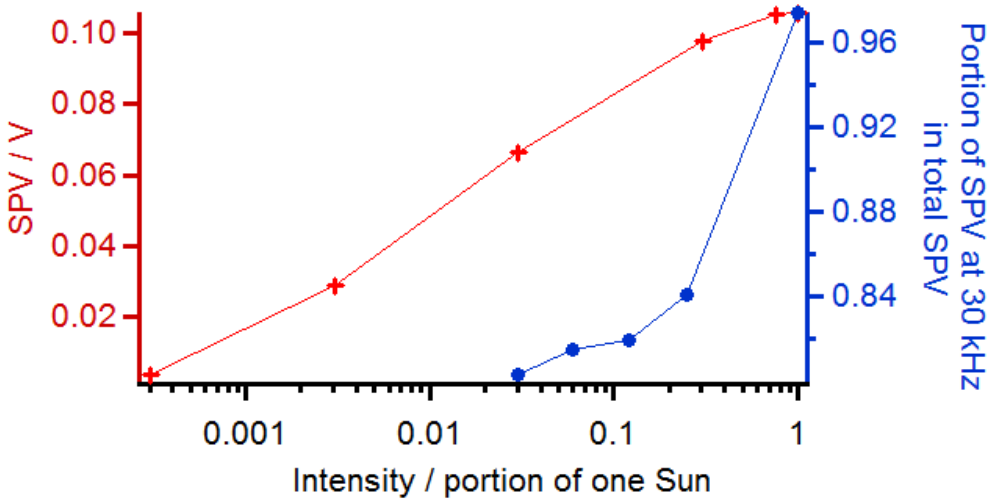

Figure 3.10 On the left axis is the SPV. On the right axis is protion of SPV at 30 kHz in total SPV, which is the ratio of time averaged SPV measured at 30 kHz over SPV when light stays on.

3.4 Conclusion

We have studied the transient surface photovoltage decay in SKPM setup by modulating probing light under different background light intensities. By comparing with the TPV data, we learned that the faster decay of SPV at higher background intensities is due to the density dependent charge carrier lifetime. The carrier lifetime would only represent the fast decay in SPV when probing intensity is high enough (>25% sun). We look forward to optimizing the intensity ratio of background vs. probing illumination to maximize S/N under the SKPM setup in the near future. Results shown in this chapter would provide a new tool for the organic photovoltaic community to understand the charge carrier lifetime under the SKPM setup, without top contact, in contrast with the normal device structure.

3.5 References:

1. Z. C. He, C. M. Zhong, S. J. Su, M. Xu, H. B. Wu and Y. Cao, *Nature Photonics*, 2012, **6**, 591-595.
2. K. M. Knesting, H. X. Ju, C. W. Schlenker, A. J. Giordano, A. Garcia, O. L. Smith, D. C. Olson, S. R. Marder and D. S. Ginger, *Journal of Physical Chemistry Letters*, 2013, **4**, 4038-4044.
3. E. L. Ratcliff, A. Garcia, S. A. Paniagua, S. R. Cowan, A. J. Giordano, D. S. Ginley, S. R. Marder, J. J. Berry and D. C. Olson, *Advanced Energy Materials*, 2013, **3**, 647-656.
4. F. Etzold, I. A. Howard, R. Mauer, M. Meister, T.-D. Kim, K.-S. Lee, N. S. Baek and F. Laquai, *Journal of the American Chemical Society*, 2011, **133**, 9469-9479.

5. J. A. Bartelt, Z. M. Beiley, E. T. Hoke, W. R. Mateker, J. D. Douglas, B. A. Collins, J. R. Tumbleston, K. R. Graham, A. Amassian, H. Ade, J. M. J. Frechet, M. F. Toney and M. D. McGehee, *Advanced Energy Materials*, 2013, **3**, 364-374.

6. B. A. Collins, J. E. Cochran, H. Yan, E. Gann, C. Hub, R. Fink, C. Wang, T. Schuettfort, C. R. McNeill, M. L. Chabinyc and H. Ade, *Nature Materials*, 2012, **11**, 536-543.

7. D. M. DeLongchamp, R. J. Kline and A. Herzing, *Energy & Environmental Science*, 2012, **5**, 5980-5993.

8. A. Rao, P. C. Y. Chow, S. Gelinas, C. W. Schlenker, C. Z. Li, H. L. Yip, A. K. Y. Jen, D. S. Ginger and R. H. Friend, *Nature*, 2013, **500**, 435-+.

9. D. C. Coffey and D. S. Ginger, *Nat Mater*, 2006, **5**, 735-740.

10. C. Groves, O. G. Reid and D. S. Ginger, *Accounts of Chemical Research*, 2010, **43**, 612-620.

11. T. Takahashi, *Jpn J Appl Phys*, 2011, **50**.

12. B. C. O'Regan, K. Bakker, J. Kroeze, H. Smit, P. Sommeling and J. R. Durrant, *Journal of Physical Chemistry B*, 2006, **110**, 17155-17160.

13. C. G. Shuttle, A. Maurano, R. Hamilton, B. O'Regan, J. C. de Mello and J. R. Durrant, *Applied Physics Letters*, 2008, **93**.

CURRICULUM VITAE

Education

PhD Physical Chemistry	University of Washington, Seattle March, 2014 Supervised by Prof. David S. Ginger
Bachelor of Science	Peking University, P. R. China, 2008 Thesis supervised by Prof. Yan Li

Publications

Probing Charge Recombination at the Buried Interface in Organic Photovoltaics
Guozheng Shao, Micah Glaz, Huanxin Ju, David S. Ginger, in preparaion

Thermodynamics *vs.* Kinetics: Understanding the Driving Energy of Charge Generation in OPVs
Guozheng Shao, Michael Salvador, Cody W. Schlenker, David S. Ginger, in preparation

Correlating the Structure of Composite Semiconducting Nanoparticles to Photocurrent Generation using Contrast Variation SANS and Photoconductive AFM
Jeffrey J. Richards, Curtis L. Whittle, **Guozheng Shao**, Danilo C. Pozzo, submitted

Morphology Dependent Trap Formation in Bulk Heterojunction Photodiodes
Guozheng Shao, Glennis E. Rayermann, Eric Smith, David S. Ginger, *the Journal of Physical Chemistry B* 2013*,* 117, 4654 (Paul Barbara Memoir Issue)

Submicrosecond Time Resolution Atomic Force Microscopy for Probing Nanoscale Dynamics
Rajiv Giridharagopal, Glennis E. Rayermann, **Guozheng Shao**, David T. Moore, Obadiah G. Reid, David S. Ginger, *Nano Letters* 2012, 12, 893

New SPM Techniques for Analyzing OPV Materials
Rajiv Giridharagopal, **Guozheng Shao**, Chris Groves, David S. Ginger, *Materials Today* 2010, 13, 50

Presentations

April, 2013	Oral presentation at Material Society Meeting of Spring 2013, San Francisco, CA
January, 2013	Oral presentation at Department of Chemistry, Peking University, Beijing, China
December, 2012	Poster presentation at Materials Society Meeting of Winter 2012, Boston, MA
September, 2012	Poster presentation at ORCAS conference of 2012, Friday Harbor, WA
June, 2010	Poster presentation at Gordon Research Conference, Mt. Holyoke College, MA

Awards

November, 2012	Departmental International Travel Award
September, 2012	Graduate Travel Award